

COOL-LAMPS VIII: Known wide-separation lensed quasars and their host galaxies reveal a lack of evolution in M_{BH}/M_{\star} since $z \sim 3$

AIDAN P. CLOONAN  ^{1, 2, 3} GOURAV KHULLAR  ⁴ KATE A. NAPIER  ⁵ MICHAEL D. GLADDERS  ^{1, 2}
 HÅKON DAHLE  ⁶ RILEY ROSENER  ¹ JAMAR SULLIVAN JR.  ¹ MATTHEW B. BAYLISS  ⁷ NATHALIE CHICOINE  ¹,
 ISAIAH ESCAPA  ¹ DIEGO GARZA  ^{1, 8} JOSH GARZA  ¹ ROWEN GLUSMAN  ^{1, 9} KATYA GOZMAN  ¹⁰
 GABRIELA HORWATH  ¹ ANDI KISARE  ¹ BENJAMIN C. LEVINE  ^{1, 11} OLINA LIANG, ¹ NATALIE MALAGON  ¹
 MICHAEL N. MARTINEZ  ¹² ALEXANDRA MASEGIAN  ^{1, 13} OWEN S. MATTHEWS ACUÑA  ¹⁴ SIMON D. MORK  ¹,
 KUNWANHUI NIU  ¹ M. RILEY OWENS  ⁷ YUE PAN  ^{1, 15} JANE R. RIGBY  ¹⁶ KEREN SHARON  ⁵
 ISAAC SIERRA  ¹ ANTONY A. STARK  ¹⁷ EZRA SUKAY  ¹⁸ MARCOS TAMARGO-ARIZMENDI  ¹ KIYAN TAVANGAR  ¹³,
 RAUL TEIXEIRA  ¹ KABELO TSIANE  ¹ GRACE WAGNER  ¹ ERIK A. ZABOROWSKI  ^{1, 19, 20} YUNCHONG ZHANG  ^{1, 4},
 AND YIFAN "MEGAN" ZHAO 

¹ Department of Astronomy and Astrophysics, University of Chicago, 5640 South Ellis Avenue, Chicago, IL 60637, USA

² Kavli Institute for Cosmological Physics, University of Chicago, 5640 South Ellis Avenue, Chicago, IL 60637, USA

³ Department of Astronomy, University of Massachusetts, 710 North Pleasant Street, Amherst, MA 01003, USA

⁴ Department of Physics and Astronomy and Pitt PACC, University of Pittsburgh, Pittsburgh, PA 15260, USA

⁵ Department of Astronomy, University of Michigan, 1085 S. University Ave, Ann Arbor, MI 48109, USA

⁶ Institute of Theoretical Astrophysics, University of Oslo, P.O. Box 1029, Blindern, NO-0315 Oslo, Norway

⁷ Department of Physics, University of Cincinnati, Cincinnati, OH 45221, USA

⁸ Department of Astronomy and Astrophysics, University of California, Santa Cruz, CA 95064, USA

⁹ Institute of Physics, University of Amsterdam, Science Park 904, 1098 XH Amsterdam, Netherlands

¹⁰ Department of Astronomy, University of Michigan, 1085 S. University Ave, Ann Arbor, MI, 48109-1107, USA

¹¹ Department of Physics and Astronomy, Stony Brook University, 100 Nicolls Rd, Stony Brook, NY 11794, USA

¹² Department of Physics, University of Wisconsin, Madison, 1150 University Avenue, Madison, WI 53706, USA

¹³ Department of Astronomy, Columbia University, 538 West 120th Street, New York, NY 10027, USA

¹⁴ Department of Astronomy, University of Wisconsin, Madison, WI 53706, USA

¹⁵ Department of Astrophysical Sciences, Princeton University, 4 Ivy Ln, Princeton, NJ 08544, USA

¹⁶ Astrophysics Science Division, Code 660, NASA Goddard Space Flight Center, 8800 Greenbelt Rd., Greenbelt, MD 20771, USA

¹⁷ Center for Astrophysics / Harvard & Smithsonian, 60 Garden St, Cambridge, MA 02138, USA

¹⁸ Department of Physics and Astronomy, Johns Hopkins University, 3400 N. Charles Street, Baltimore, MD 21218, USA

¹⁹ Department of Physics, The Ohio State University, Columbus, OH 43210, USA

²⁰ Center for Cosmology and Astro-Particle Physics, The Ohio State University, Columbus, OH 43210, USA

Submitted to ApJ

ABSTRACT

Wide-separation lensed quasars (WSLQs) are a rare class of strongly lensed quasars, magnified by foreground massive galaxy clusters, with typically large magnifications of the multiple quasar images. They are a relatively unexplored opportunity for detailed study of quasar host galaxies. The current small sample of known WSLQs has a median redshift of $z \approx 2.1$, larger than most other samples of quasar host galaxies studied to date. Here, we derive precise constraints on the properties of six WSLQs and their host galaxies, using parametric surface brightness fitting, measurements of quasar emission lines, and stellar population synthesis of host galaxies in six WSLQ systems. Our results, with significant uncertainty, indicate that these six hosts are a mixture of star-forming and quiescent galaxies. To probe for co-evolution between AGNs and host galaxies, we model the offset from the ‘local’ ($z = 0$) $M_{\text{BH}} - M_{\star}$ relation as a simple power-law in redshift. Accounting for selection effects, a

WSLQ-based model for evolution in the $M_{\text{BH}} - M_{\star}$ relation has a power-law index of $\gamma_M = -0.42 \pm 0.31$, consistent with no evolution. Compared to several literature samples, which mostly probe unlensed quasars at $z < 2$, the WSLQ sample shows less evolution from the local relation, at $\sim 4\sigma$. We find that selection effects and choices of M_{BH} calibration are the most important systematics in these comparisons. Given that we resolve host galaxy flux confidently even from the ground in some instances, our work demonstrates that WSLQs and highly magnified AGNs are exceptional systems for future AGN–host co-evolution studies.

Keywords: Galaxy Evolution (594) — Quasars (1319) — Supermassive Black Holes (1663) — AGN Host Galaxies (2017) — Strong Gravitational Lensing (1643)

1. INTRODUCTION

At their gravitational centers, galaxies contain supermassive black holes (SMBHs), the mass (M_{BH}) of which is known to correlate with other physical properties of galaxies, such as the stellar mass (M_{\star} ; e.g., Magorrian et al. 1998; Häring & Rix 2004), the stellar velocity dispersion of the bulge (e.g., Ferrarese & Merritt 2000), and the host galaxy luminosity (e.g., Marconi & Hunt 2003). These relations reflect an underlying cosmological history of co-evolution between SMBHs and their host galaxies (e.g., Kormendy & Ho 2013). Accretion of matter from the surrounding galaxy onto the SMBH fuels outflows of gas and radiation, which we observe from various inclination angles as active galactic nuclei (AGNs), according to the ‘unified model’ (Antonucci 1993; Netzer 2015; Ogawa et al. 2021). From a theoretical perspective, due to the highly energetic nature of accretion-powered outflows, we might anticipate a co-evolutionary relationship between AGNs and galaxies. Indeed, theoretical works have continuously hypothesized an ‘AGN feedback’ scenario, in which AGN activity plays a significant role in regulating star formation activity in massive galaxies (Bower et al. 2006; Croton et al. 2006; Hopkins et al. 2006; Somerville et al. 2008; Habouzit et al. 2021; Wellons et al. 2023).

From an observational perspective, the details of the co-evolutionary relationship between AGNs and their host galaxies are poorly understood (for some reviews, see Fabian 2012; King & Pounds 2015; Padovani et al. 2017; Veilleux et al. 2020; Sajina et al. 2022). Unobscured quasars—viewed at an angle such that the accretion disk is directly visible—are extremely luminous (Lynden-Bell 1969) and can outshine their host galaxies by orders of magnitude in the optical and near-infrared (NIR) regime (Hopkins et al. 2006). This large relative difference in surface brightness significantly limits the ability to spatially resolve and study their host galaxies even at low redshift (Bahcall et al. 1997). We effectively observe distant quasars as point sources.

Disentangling quasar flux from host flux requires high signal-to-noise (S/N) and/or resolution. Since unobscured quasars are very luminous in the UV through mid-IR, millimeter observations such as from ALMA provide better contrast of molecular outflows and cold gas in the host galaxy against radiative flux from the quasar (e.g., Omont et al. 1996; Wagg et al. 2012; Venemans et al. 2017). Combining integral field spectroscopy and adaptive optics has significantly improved ground-based mapping of quasar outflows (Kakkad et al. 2023). Furthermore, despite persistent observational difficulties in PSF modeling and quasar–host decomposition (Zhuang & Shen 2023), space-based observatories have allowed for much clearer detection and study of quasar host galaxies. *HST* observations of quasars at lower redshift ($z \lesssim 0.5$) have found that the host galaxies vary in morphology from early- to late-type galaxies (Dunlop et al. 2003; Guyon et al. 2006) and that they can have regions with large star formation rates (Young et al. 2014). *HST* additionally facilitated the first cosmological studies of co-evolution between AGNs and host galaxies over redshift (Peng et al. 2006; Merloni et al. 2010). Recently, early studies with *JWST* are probing gas, star formation, and accretion-driven outflows around distant quasars (Ding et al. 2022; Kocevski et al. 2023; Cresci et al. 2023) and further surpassing previous observational constraints to study AGNs and their environments near the end of cosmic reionization (Furtak et al. 2023; Marshall et al. 2023; Larson et al. 2023; Pacucci et al. 2023; Wang et al. 2023) and even earlier to $z \sim 10$ (Bogdán et al. 2023; Goulding et al. 2023).

The aforementioned scaling relations between SMBH and host galaxy properties were established using relatively local samples ($z \lesssim 0.1$; Häring & Rix 2004). Extending these scaling relations to high redshift to study cosmic evolution is an ongoing problem (e.g., Suh et al. 2020; Ding et al. 2020; Li et al. 2023; Pacucci et al. 2023; Tanaka et al. 2024). Not only are host galaxies even more difficult to observe, but the masses of quasar SMBHs are often constrained with secondary scaling re-

lations derived from quasar emission (e.g., Wandel et al. 1999; Vestergaard 2002; Mejia-Restrepo et al. 2016) rather than a physically motivated model. Reverberation mapping reduces uncertainty in SMBH mass measurements significantly, but is almost entirely restricted to unobscured AGNs at $z < 1$ (Li et al. 2023). Selection bias is another enormous challenge. Since AGN luminosity is explicitly related to SMBH mass (Marconi et al. 2004), all flux- or luminosity-limited sample selections inevitably bias the parameter space(s) of interest (Lauer et al. 2007; Schulze & Wisotzki 2011).

Strong gravitational lensing of background quasars provides several opportunities to overcome the above challenges. Notably, it provides effective spatial resolution of quasar host galaxies at $z > 1$ in optical and IR imaging (Bayliss et al. 2017). While a lensed quasar still appears as a point source, the lens stretches and magnifies the host galaxy light, separating quasar and host galaxy flux on the sky.

Nearly all known strongly lensed quasars—several hundred in total—are lensed by single galaxies (Lemon et al. 2023). Angular image separations between the lens galaxy and lensed quasar in these systems are typically $\sim 1''$. There are eight known lensed quasars with image separations greater than $10''$, each lensed by a massive galaxy cluster (Inada et al. 2003, 2006; Dahle et al. 2013; Shu et al. 2018, 2019; Martinez et al. 2023; Napier et al. 2023b; Kisare et al. in prep.). We refer to these systems as *wide-separation lensed quasars* (WSLQs). Previous studies have used quasars that are strongly lensed by galaxies to study quasar–host co-evolution over cosmic time, as far back as redshift $z \sim 4.5$ (e.g., Peng et al. 2006; Stacey et al. 2020; Ding et al. 2021). However, strong lensing by galaxy clusters provides much higher magnification and larger image separation, better separating the flux from the quasar and host galaxy than galaxy-scale lensing does. Recent studies of WSLQs, motivated by the larger magnification and better natural resolution, have focused on radio emission (McKean et al. 2021; Hartley et al. 2021), quasar variability and structure (Williams et al. 2021a,b; Hutsemékers et al. 2023; Fian et al. 2024), and cosmology (Napier et al. 2023a).

In this work, using archival and new imaging and spectroscopy from *HST*, Keck Observatory, the Magellan Telescopes, and the Nordic Optical Telescope (NOT), we study the quasar and host galaxy properties in six of the known WSLQ systems, for which we have reliable detections of host galaxy flux. (The remaining two are not detected in extant data.) This WSLQ sample spans a redshift range of $1.5 < z < 3.3$. With constraints on the physical properties, we model the $M_{\text{BH}}-M_{\star}$ relation

and study its evolution with redshift, as a probe of co-evolution between AGNs and galaxies, while accounting for selection bias and other systematics.

This paper is organized as follows. In Section 2, we outline a combination of archival data and new observations used for analysis of each WSLQ. In Section 3, we describe methodologies for modeling quasar and galaxy properties. Section 4 discusses the $M_{\text{BH}}-M_{\star}$ relation and the implications of our modeling results. In particular, we directly compare to samples at different cosmological epochs from the literature. Then, Section 5 investigates several important sources of bias to qualify the key measurements. We discuss takeaways and physical interpretations of these various analyses in Section 6. Finally, we summarize our work and our conclusions in Section 7.

Magnitudes are reported in the AB system. For all geometric and cosmological calculations, we assume a flat ΛCDM cosmology with $\Omega_{\Lambda} = 0.7$, $\Omega_m = 0.3$, and $H_0 = 70 \text{ km s}^{-1} \text{ Mpc}^{-1}$.

2. TARGETS AND OBSERVATIONAL DATA

The name of each WSLQ is given in Table 1, and images are shown in Figure 1. For brevity, in the rest of this paper, we abbreviate each WSLQ with an initial and four numbers, e.g. SDSS J1004+4112 as SJ1004.

We use a combination of archival and new observations in this work. To carry out any robust analysis of a galaxy hosting a luminous AGN, a detection (with convincingly high signal-to-noise) of extended flux beyond the point source of an AGN is required. While *HST* imaging easily detects flux from WSLQ host galaxies, only three known WSLQs have previously existing *HST* imaging (Inada et al. 2005; Oguri et al. 2013; Sharon et al. 2017), with a fourth in preparation (GO-17243, PI: Napier) and a fifth to be visited in the coming months (GO-17431, PI: Gladlers). Host galaxy detection with ground-based observations at optical wavelengths requires longer exposures (Martinez et al. 2023), a challenge which guides observation planning and selection of archival data. Each of the six WSLQs and a summary of all of the observational data used for analysis is listed in Table 1.

2.1. Archival Observations

For photometry of each of SJ1004, SJ1029, and SJ2222, we use *HST* WFC3 and/or ACS imaging in the observed-frame optical and NIR. *HST* imaging came through GO-10509 (PI: Kochanek), GO-9744 (PI: Kochanek), and GO-10793 (PI: Gal-Yam) for SJ1004; through GO-12195 (PI: Oguri) for SJ1029; and through GO-13337 (PI: Sharon) for SJ2222. The SDSS extended Baryon Oscillation Spectroscopic Survey (eBOSS) provides calibrated spectra of resolution $R \sim 2000$ (Smee

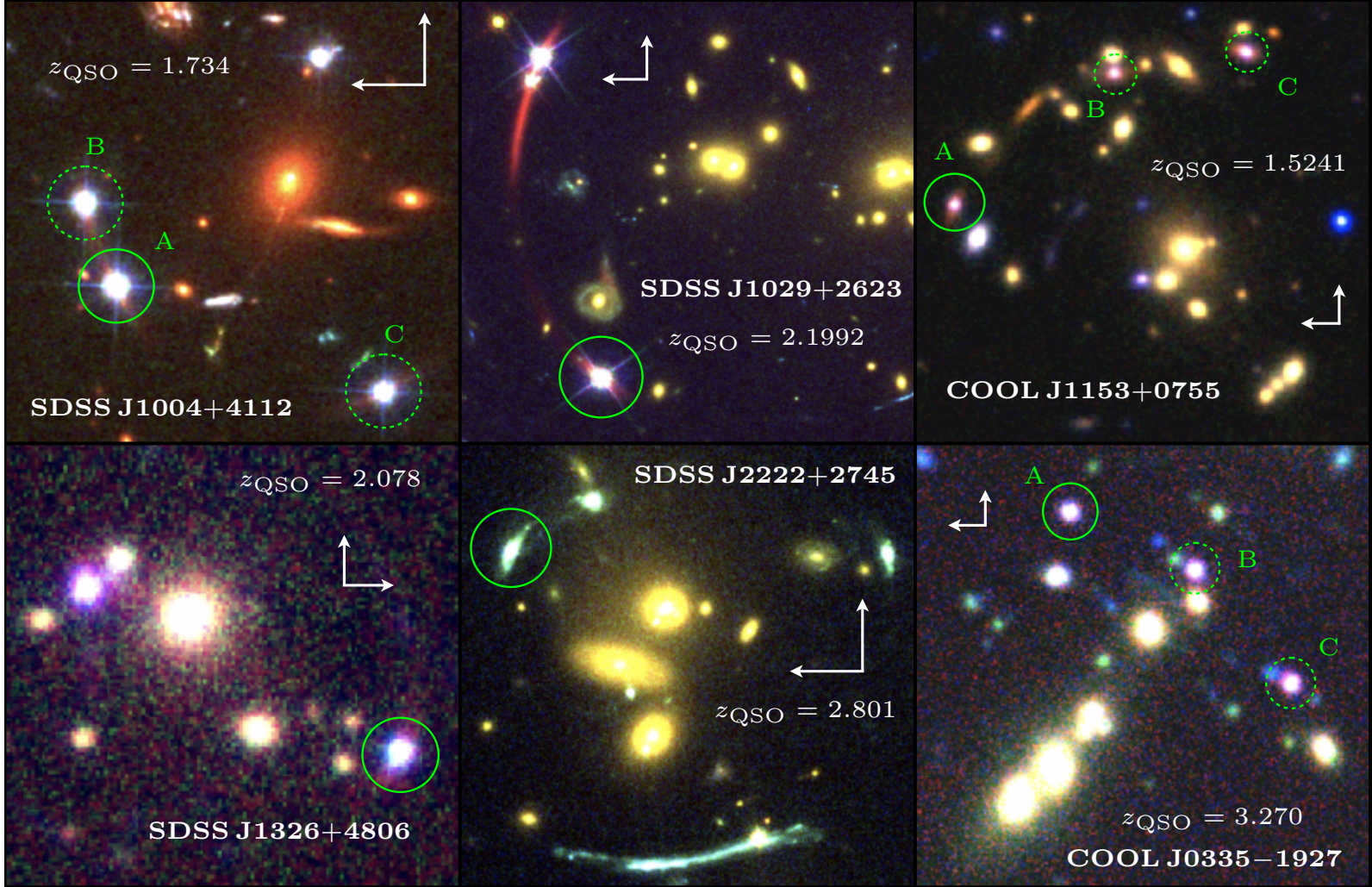


Figure 1. RGB images of each WSLQ system. The quasar images analyzed in this work are circled in green, with primary images labeled as ‘A’ or with a solid circle. For the WSLQs where we later measure the properties of multiple images, the additional quasar images are shown with dotted circles. Each quasar redshift and line-of-sight name is given in the figure. A scale of $3''$ is given in each cutout with a pair of white arrows marking the North and East directions (where North is always clockwise of East).

et al. 2013; Dawson et al. 2016) for SJ1004, SJ1029, and SJ1326. SJ1029 was also observed on December 15, 2007 (Program C245L, PI: Ofek) with the Low Resolution Imaging Spectrometer (LRIS) at Keck Observatory (Oke et al. 1995). We use this archival spectrum for SJ1029 as it has higher signal-to-noise (S/N) than eBOSS, and we use eBOSS spectra for SJ1004 and SJ1326. We do not perform spectroscopic analysis of SJ2222, as there exists a robust measurement of M_{BH} via reverberation mapping (Williams et al. 2021a,b).

We carry out wavelength- and flux-calibrations for LRIS spectroscopy of SJ1029 using standard IRAF tools (Tody 1986). The LRIS spectrum is flux-calibrated to the corresponding eBOSS spectrum of the object to ensure accuracy and minimize uncertainty in the calibra-

tion process overall. This results in a calibrated spectrum of eBOSS’s resolution but with higher S/N.

2.2. New Observations

We conducted observations of SJ1326 with NOT and of CJ0335 and CJ1153 with the Magellan Telescopes. Below, we describe observing for each; in particular, we also briefly introduce the CJ1153 system, as it contains a previously unreported WSLQ. We performed all reductions, including image stacking and spectral flux/wavelength calibrations, using IRAF (Tody 1986).

2.2.1. SDSS J1326+4806

We have a calibrated optical spectrum of SJ1326 from eBOSS. From NOT imaging programs for host galaxy photometry, we detect host galaxy flux in g , H , and K_S

Name	RA	Dec	z_{lens}	z_{QSO}	Imaging Data	Spectroscopic Data	Discovery Reference
SJ1004	151.1429	41.2118	0.68	1.734	<i>HST</i> F435W, F555W, F814W, F160W; <i>Spitzer</i> IRAC Ch1–4	eBOSS	Inada et al. (2003)
SJ1029	157.3077	26.3917	0.584	2.1992 ^a	<i>HST</i> F475W, F814W, F160W	Keck LRIS	Inada et al. (2006)
SJ2222	335.5354	27.7594	0.49	2.801 ^b	<i>HST</i> F435W, F606W, F814W, F160W	n/a ^c	Dahle et al. (2013)
SJ1326	201.5001	48.1121	0.396	2.078	NOT <i>gHKs</i>	eBOSS	Shu et al. (2019)
CJ0335	53.7701	−19.4688	0.4178	3.27	Magellan <i>grzH</i>	Magellan LDSS3-C	Napier et al. (2023b)
CJ1153	178.3302	7.9325	0.42	1.5241	Magellan <i>grzJHKs</i>	Magellan LDSS3-C	Kisare et al. (in prep.)

^a Updated redshift from Acebron et al. (2022a).

^b Updated redshift from Acebron et al. (2022b).

^c SJ2222 has a measurement for M_{BH} from reverberation mapping (Williams et al. 2021a,b)

Table 1. The sample of wide-separation lensed quasars and the data used for each. Redshifts are taken from the given discovery reference for SJ1004 and SJ1326, and from Acebron et al. (2022a,b) for SJ1029 and SJ2222 respectively. Imaging of SJ1326 is from the Nordic Optical Telescope (NOT), while imaging and spectroscopy of CJ0335 and CJ1153 are from the Magellan Telescopes.

filters. The g -band detection is part of an ongoing monitoring program with NOT/ALFOSC to measure time-delays between quasar images for cosmological study. The total exposure time is 14290s, from a stack of 56 single-epoch images. Then, we observed SJ1326 in K_S on April 27, 2021 with NOT/NOTCAM for 3600s of total exposure as part of Program 63-017 (PI: Dahle). Observations in H -band were taken on March 3, 2023 as part of Program 66-011 (PI: Dahle), with an exposure time of 3564s.

2.2.2. COOL J0335–1927

As in Napier et al. (2023a), we use photometric and spectroscopic observations from Magellan Clay/LDSS3-C, taken on September 18, 2022 and on Feb 1, 2023. The total combined integration times from both nights were 1080s in the g and r filters and 720s in the z filter. We use the same reduced grz imaging in this paper. To measure flux around the Balmer break (rest-frame 4000 Å), we observed of CJ0335 in H -band with Baade/FOURSTAR on December 10, 2022, with a total integration time of 1310s.

2.2.3. COOL J1153+0755

CJ1153 is a previously unreported WSLQ system, the most recently discovered by the COOL-LAMPS collaboration (Khullar et al. 2021) as a continuation of its lensed quasar search (Martinez et al. 2023; Napier et al. 2023a). We briefly describe the system here, but we will defer to an upcoming paper Kisare et al. (in prep.) for a more detailed analysis of its properties. The CJ1153 line of sight includes a massive galaxy cluster—detected in a joint X-ray–Sunyaev-Zeldovich survey by Tarrío et al. (2019)—which strongly lenses a group of galaxies at $z \sim 1.5$. This lensed group includes the quasar-hosting

galaxy CJ1153. The quasar, lensed group, lensing cluster and other various lensed sources will be imaged by *HST* in Cycle 31 Program GO-17431 (PI: Gladders).

Imaging in $grzJHKs$ filters and spectroscopy of CJ1153 were collected over the course of several Magellan nights in early 2023: February 1, February 6, March 9, and March 24. The total exposure time for grz imaging (Clay/LDSS3-C; Feb. 1 and Mar. 24) was 540s per filter, while for $JHKs$ (Baade/FOURSTAR; Feb. 6 and Mar. 9) we obtained total exposure times of 3429s for J and 3493s each for H and K_S . Optical spectroscopy for each quasar image was acquired via Magellan Clay/LDSS3-C (Feb. 1 and Mar. 24).

3. MEASUREMENTS AND ANALYSIS

3.1. Quasar–Host Photometry

To constrain host galaxy properties, we begin by constructing surface brightness (SB) profiles of the lensed quasars and their host galaxies using GALFIT (Peng et al. 2002, 2010). GALFIT performs parametric modeling of SB profiles for astronomical sources. The code allows for least-squares fitting of complex light profiles consisting of multiple sources or components. We carry out quasar–host decomposition by simultaneously measuring quasar and host magnitudes and fitting nearby contaminants along the line of sight. An example GALFIT model is shown in Figure 2. For each WSLQ, the process for photometry with GALFIT is as follows:

1. We construct a model PSF for each imaging filter. (A more detailed explanation is given in the next paragraph.)
2. With a PSF as an input, for each filter, we optimize a GALFIT model of the line of sight around

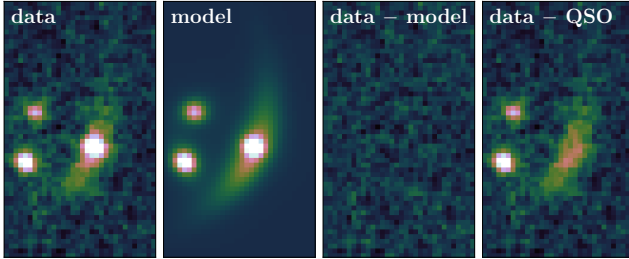


Figure 2. GALFIT SB model of SJ1326 in the K_S filter, observed with NOT. From left to right: reduced K_S image, SB model fit to the image, model residual, reduced image with model quasar subtracted. Note that this decomposition appears sufficient for measuring host galaxy photometry even with ground-based imaging.

the quasar image. The quasar and foreground stars are each fit with a single point source, while host galaxy arcs, lensing cluster galaxies, and other contaminating sources are fit with one or more Sérsic profiles.

3. We quantify noise in the image by computing a root-mean-square (RMS) map of the optimized model residual. (i.e. image minus GALFIT model, such as in the third panel of Figure 2.) This RMS map is then smoothed by a 2D Gaussian kernel, which is symmetric with a size of 3σ .
4. We generate an array of mock images by multiplying each of 1000 unitary random Gaussian fields by the smoothed RMS map, and then adding the optimized GALFIT model.
5. Finally, we propagate uncertainty on the host galaxy flux measurement by re-optimizing the GALFIT model on each of these 1000 mock fields, providing a probability distribution function for host galaxy flux.

PSF modeling for *HST* imaging is different from that for ground-based imaging; we briefly summarize the two techniques here. For an *HST* image, we identify a set of stars of ‘medium’ brightness, i.e., those which neither oversaturate the CCDs nor are very faint. The images of stars are stacked, and each input image is azimuthally filtered about the center and at larger radii, to minimize contamination from nearby sources. Then, we optimize a basic Sérsic model for each diffraction spike (with the stacked image subtracted) and then add the spike models to the stacked image, giving an empirical PSF. For a ground-based image, we directly construct a model PSF by fitting one or more Moffat profiles (Moffat 1969) to a non-saturated reference star in the line of sight.

For ground-based images of SJ1326, CJ0335, and CJ1153, we empirically measure magnitude zeropoints

in order to properly calibrate quasar and host galaxy magnitude measurements into the AB system. Either manually or using **SExtractor** (Bertin & Arnouts 1996), we carry out aperture photometry on bright stars near the line of sight, convert the resulting flux into a magnitude, and then measure the zeropoint by adding the resulting magnitude to an existing calibrated measurement in a catalog. We use 2MASS catalogs (which have Vega magnitudes, requiring a final filter-dependent translation to AB; Skrutskie et al. 2006) for NIR filters and archival DESI Legacy Surveys for optical filters.

Our method with GALFIT provides calibrated flux measurements of the quasars and host galaxies in the image plane. In the strong gravitational lensing regime, the demagnified flux in the source plane is directly proportional to the flux in the image plane as $f_{\text{source}} = \mu_m f_{\text{image}}$, where μ_m is the magnification coefficient for the lensed image. To demagnify flux into the source plane, we use magnification coefficients reported in Napier et al. (2023a,b) for SJ1004, SJ1029, SJ2222, and CJ0335. For SJ1326 and CJ1153, we use magnifications computed from ground-based lens models (to be described by Kisare et al. in prep.) following the procedure of Napier et al. (2023b), which are less precise than models based on *HST* imaging (Sharon et al. 2017). All lens models and magnification maps were constructed using the lens modeling software **Lenstool** (Jullo et al. 2007).

3.2. Stellar Population Synthesis Modeling

We employ stellar population synthesis (SPS) to constrain host galaxy stellar masses and spectral energy distributions (SEDs). Using **Prospector** (Johnson et al. 2021), we implement a parametric treatment of star formation using a ‘delayed-tau’ model, where star formation rate (SFR) follows a ‘delayed’ exponential decay as a function of time, i.e., $\text{SFR}(t) \propto t e^{-t/\tau}$ where τ is a free parameter. For these parametric models, **Prospector** samples in the parameter space of mass, age, and the folding timescale τ .

While SPS provides remarkably powerful tools for inferring physical properties of unresolved stellar populations, we note two critical caveats in the approach. First and foremost, in galaxy SED modeling, one usually has to make critical assumptions about the star formation history (SFH). The choice of parametric SFH may bias stellar mass measurements by up to 0.2 – 0.5 dex (Carnall et al. 2019), depending on the model and on the type of galaxy (star-forming/quiescent). The second is the age-metallicity-dust degeneracy (e.g., Conroy 2013). These problems are well known, and we must look to

minimize their impacts on our measurements. We discuss SED modeling systematics in Section 5.2.

As outlined previously, the number of photometric filters in which the host galaxy is robustly detected varies from system to system. With that in mind, we approach SPS modeling for each WSLQ system differently in an attempt to minimize systematic bias. For all stellar population modeling, we assume a Chabrier initial mass function (IMF; Chabrier 2003) and the dust attenuation law from Calzetti et al. (2000).

Depending on how well a model constrains the stellar mass, we change the array of free parameters in a given SPS model, either including additional free parameters or fixing parameters. At the very least, we look to constrain total stellar mass $M_{\star,\text{tot}}$, galaxy age t_{age} , e -folding timescale τ , and the optical depth from diffuse interstellar dust $\tau_{\lambda,2}$ with each SED template. While we prefer to change a model slightly to align with what a galaxy's photometry can capably constrain, we recognize that this heterogeneity in modeling can introduce bias in key inferred parameters. We include a simple test for this concern in Section 5.2. Note that in the formalism described above, the remnant stellar mass corresponds to the galaxy mass contained in stars, once corrected for mass loss via stellar winds and supernova feedback. The term ‘stellar mass’ M_{\star} refers specifically to the remnant stellar mass throughout the rest of this paper.

Below, we outline our model choices and setup for each quasar host galaxy. With the exception of SJ1004, we use GALFIT photometry as described in Section 3.1.

SDSS J1004+4112. Ross et al. (2009) compute and report demagnified flux values for the host galaxy of SJ1004 in 8 total imaging filters, four from *HST* (optical and NIR) and four from *Spitzer* IRAC (mid-IR). This *HST+Spitzer* imaging remains the highest quality data available for this WSLQ. As such, we use the fluxes from Ross et al. (2009) and recalculate the demagnified flux in each filter using the updated lens model from Napier et al. (2023a).

In addition to $M_{\star,\text{tot}}$ and t_{age} , we fit for τ , $\tau_{\lambda,2}$, and stellar metallicity $\log(Z/Z_{\odot})$. Given the larger constraining power from 8 photometric filters, we include NIR dust emission (as a nuisance parameter), nebular continuum, and line emission in the model. The dust emission comes from the heating of dust grains by rest-UV photons. Physically, the nebular emission arises from interstellar gas, which is characterized by an ionization parameter U and gas-phase metallicity Z_{gas} . We let ionization U be a free parameter and keep gas-phase metallicity fixed at $\log(Z_{\text{gas}}/Z_{\odot}) = 0$. Finally, we also introduce a free ‘constant’ parameter C to the model for SJ1004, which corresponds to a fraction of the total

stellar mass formed by a ‘tophat’ term in the $\text{SFR}(t)$ function. In other words, we assume for SJ1004 that SFR follows:

$$\text{SFR}(t) \propto t \exp \left\{ -\frac{t}{\tau} \right\} + \frac{CM_{\star,\text{tot}}}{t_{\text{age}}}, \quad (1)$$

where t_{age} and $M_{\star,\text{tot}}$ are free parameters in the model.

SDSS J1029+2623. We have available imaging in three *HST* filters: F475W, F814W, and F160W. While this allows for far less flexibility in an SED template for SJ1029 than for SJ1004, the flux measurement in F160W offers an important constraint because it probes redward of the Balmer break at $z \sim 2$. As with SJ1004, we cite the image magnifications from the lens model built by Napier et al. (2023a).

We use the delayed-tau model, with $M_{\star,\text{tot}}$, t_{age} , and τ as free parameters. We fix the metallicity in stars to Z_{\odot} and impose an upper limit $\tau_{\lambda,2} < 1$ on the diffuse dust attenuation. The metallicity does not significantly impact the stellar mass measurement in this instance because the model fits the SED amplitude but not elemental abundances. Furthermore, an initial fit with a more lenient prior $\tau_{\lambda,2} < 3$ produces a dusty best-fit with $\log(M_{\star}/M_{\odot}) > 12$ and $\log(\text{SFR}/M_{\odot} \text{ yr}^{-1}) \sim 3$. We suspect this result is likely inaccurate as it implies an overly high SFR for such a massive galaxy (e.g., Somerville et al. 2008; Leja et al. 2022), and we therefore assume that the host galaxy is not highly obscured.

SDSS J2222+2745. We use *HST* imaging in the F435W, F606W, F814W, and F160W filters and a similar SPS formalism as for SJ1029. As we have improved constraining power with four filters and we also do not find an unphysical solution, we do not impose the stricter upper limit on $\tau_{\lambda,2}$. Due to its apparent bluer color, we also introduce nebular emission and continuum similarly to SJ1004. We reuse the magnification computed by Napier et al. (2023a).

SDSS J1326+4806. The SED modeling of this galaxy follows an identical process to SJ1029. The photometric filters from NOT in which we confidently detect the quasar host galaxy— g , H , and K_S —span a similar wavelength range, and the galaxy appears red in those colors as shown in Figure 1. A model galaxy with strong dust attenuation is again overly massive and highly star-forming, and so we again assume impose an upper limit of $\tau_{\lambda,2} < 1$, keeping $M_{\star,\text{tot}}$, $\tau_{\lambda,2}$, t_{age} , and τ as free parameters. The image magnifications are determined from a simpler lens model based on the available ground-based imaging, using a similar methodology as in Martinez et al. (2023) and Napier et al. (2023b).

COOL J0335–1927. We have one more photometric detection ($grzH$) than for SJ1029 and SJ1326, and we do not find any possibly unphysical best-fits with a

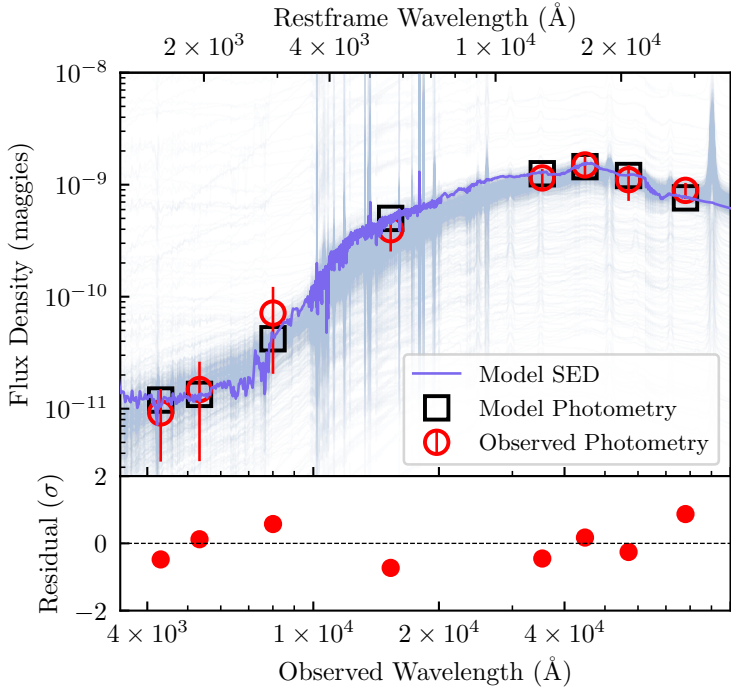


Figure 3. SED model for the host galaxy of SJ1004. The light-blue band is a set of random samples from the output sampling chain give by the SPS framework. On the bottom panel we show the residuals for each filter, where we define the residual $\sigma = (m_{\text{obs}} - m)/s_m$, i.e., observed magnitude minus model magnitude divided by observed magnitude uncertainty.

lenient prior on dust attenuation. As such, we do not impose the upper limit on $\tau_{\lambda,2}$. The metallicity is kept constant at the solar value. Similarly to SJ1004, we include nebular continuum and emission as well as dust emission. We use ground-based magnification estimates of each quasar image from Napier et al. (2023a).

COOL J1153+0755. We model this quasar host galaxy using the same procedure as for CJ0335, except with metallicity $\log(Z/Z_{\odot})$ as an additional free parameter. Our set of photometric filters is similar but larger ($grzJHK_S$), and so it better samples the galaxy SED. We compute magnifications from a ground-based lens model, which will be discussed in further detail by Kisare et al. (in prep.).

3.3. Analysis of Quasar Spectroscopy

For distant AGNs, current methods for constraining M_{BH} require three key components: a measurement of velocity dispersion from the unresolved ‘broad-line region’ (BLR), a constraint on the BLR’s physical size, and an assumption that the classical virial theorem applies (Peterson 1993). If we measure the BLR radius R_{BLR} and its Doppler shift ΔV , then we find a SMBH

mass (Williams et al. 2021a,b):

$$M_{\text{BH}} = f \frac{R_{\text{BLR}} \Delta V^2}{G}, \quad (2)$$

where f is a fudge constant accounting for unknown geometry and kinematics in the BLR, and G is the universal gravitational constant. In lieu of reverberation mapping, empirical correlations between R_{BLR} and both emission and continuum luminosities have allowed for M_{BH} constraints from a single spectrum (Wandel et al. 1999; Vestergaard 2002). Although subject to additional uncertainty, these ‘single-epoch’ measurements require far less observational resources and have allowed for efficient M_{BH} measurements for large samples of quasars in surveys (e.g., Shen et al. 2011; Koss et al. 2022).

We measure the quasar SMBH mass M_{BH} via single-epoch spectroscopy of each WSLQ system except for SJ2222, for which we cite an existing M_{BH} value from reverberation mapping (Williams et al. 2021a,b).

3.3.1. Quasar Broad Emission Lines

For each quasar spectrum, using `PySpecKit`, we fit both the emission profile from the MgII broadline at $\lambda_{\text{rest}} = 2799.5$ and the surrounding continuum with a Voigt profile and a fifth-order polynomial, respectively. This fit provides a measurement of the MgII full-width-at-half-maximum (FWHM), a measurement of velocity dispersion and a continuum luminosity λL_{λ} , which correlates with R_{BLR} . `PySpecKit` is a package designed to replicate spectroscopic tools from IRAF in Python. Its core functions use a basic likelihood maximization scheme, which does not provide uncertainties on free parameters as a Markov Chain Monte Carlo (MCMC) would. However, uncertainties in the measurements of M_{BH} are dominated by intrinsic scatter in the luminosity–BLR relations we use, and so we treat the uncertainty contribution from the emission line fitting as negligible.

Regarding the choice of emission line, common choices are CIV and MgII in the rest-UV and the Balmer lines H α and H β in the rest-optical. We prefer MgII to CIV because the latter’s shape is more intrinsically impacted by outflowing, blueshifted gas, leading to systematic bias in measurements of the virialized quasar structure (Mejía-Restrepo et al. 2016). Generally speaking, the broad Balmer lines are preferred to both MgII and CIV (Shen 2016), but they are not available with (observed-frame) optical spectroscopy at redshifts $z > 1.5$.

3.3.2. Measuring SMBH Masses

Given the measurements of intrinsic quasar luminosity and of rotational velocity structure described above,

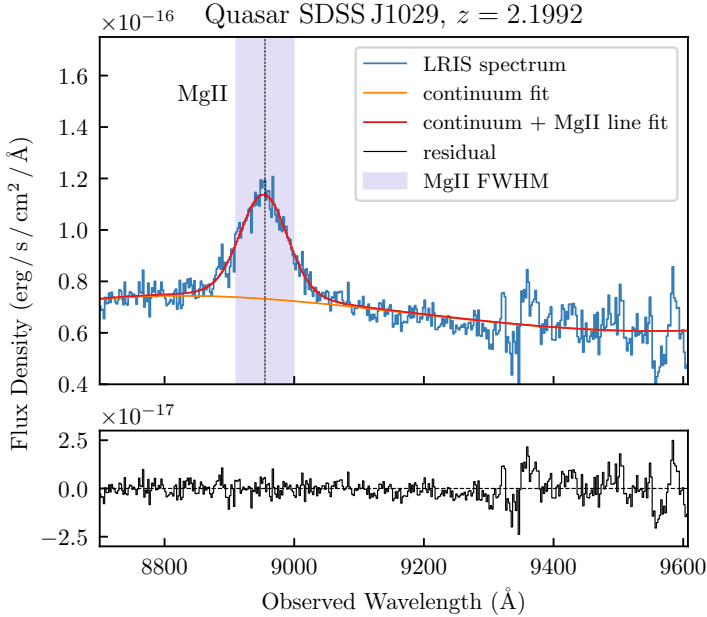


Figure 4. The spectrum surrounding the MgII broad emission line of the lensed quasar SJ1029. Note that the residual plot here is merely $(\text{data} - \text{model})$.

we adopt the framework outlined by Trakhtenbrot & Netzer (2012) to compute constraints on SMBH masses M_{BH} . Assuming that the virial theorem applies (see Equation (2)), we compute M_{BH} via their relation between the continuum luminosity $L_{3000} \equiv 3000 \cdot L_{\lambda}$, the FWHM of MgII, and M_{BH} :

$$M_{\text{BH}}(L_{3000}) = 5.60 \times 10^6 \left[\frac{L_{3000}}{10^{44} \text{ erg s}^{-1}} \right]^{0.62} \times \left[\frac{\Delta V_{\text{MgII}}}{10^3 \text{ km s}^{-1}} \right]^2 M_{\odot}, \quad (3)$$

$$\text{where } \Delta V_{\text{MgII}} = \frac{\text{FWHM} \times c}{\lambda_{\text{rest}}(1+z)} \text{ km s}^{-1}. \quad (4)$$

Trakhtenbrot & Netzer (2012) found the above relation by calibrating MgII measurements to those via H β for SDSS quasars. Regarding uncertainties, we simply adopt the scatter associated with Equation 3 of 0.33 dex, as they empirically computed. As a visualization for this process, we show the spectroscopic analysis for SJ1029 in Figure 4.

To measure M_{BH} for CJ0335, where we do not have access to MgII, we instead use the CIV emission line. However, we compute a correction to the FWHM by fitting two Gaussian components to the emission and measuring the centroid blueshift, using the method outlined by Coatman et al. (2017). This correction depends on this blueshift, which is a measurement of the centroid's offset

from the expected CIV wavelength at $z = 3.270$. This correction may not bypass the aforementioned bias with CIV-based measurements induced by blueshifted ionized gas, but it still notably reduces the intrinsic scatter in the calibration (Coatman et al. 2017).

4. RESULTS

Having measured the kinematics of quasar BLRs and constructed composite stellar populations for each host galaxy, we have constrained quasar SMBH masses and host galaxy stellar masses. With these in hand, we now investigate the $M_{\text{BH}}-M_{\star}$ relation and compare the WSLQ host galaxies to other samples of AGN-hosting galaxies in the literature. We then combine the WSLQ host galaxies with these other samples and model the change in M_{BH}/M_{\star} as a function of redshift. As is always true for galaxy evolution studies, we have no access to a longitudinal sample, and instead compare time-ordered cross-sectional samples to deduce evolutionary effects (e.g., Abramson et al. 2016). Additionally, we should note that SMBHs and galaxies only grow in mass over time, and hence shift to larger values over time in the $M_{\text{BH}}-M_{\star}$ plane. Consequentially, AGN samples at different redshifts but over similar mass ranges are not necessarily antecedents/descendants of one another.

4.1. $M_{\text{BH}}-M_{\star}$ Relation

The $M_{\text{BH}}-M_{\star}$ relation illuminates the relative growth of SMBHs and their host galaxies. For a point of comparison, we adopt the nearby AGNs at $z < 0.1$ from Bennert et al. (2015, 2021) as a representative sample of the local relation. For self-consistency, we recalibrate the SMBH masses to the Trakhtenbrot & Netzer (2012) formalism using the H β emission line properties and Eq. 3 from Trakhtenbrot & Netzer (2012), and we convert their stellar masses to a Chabrier IMF from a Kroupa IMF by subtracting 0.075 dex, a conversion that Bennert et al. (2021) use in their own analysis. We supplement this sample with the local non-active SMBH sample from Häring & Rix (2004). Following the literature (e.g., Peng et al. 2006; Kormendy & Ho 2013; Li et al. 2023), we adopt a power law relation between SMBH masses and host galaxy stellar masses for the local sample at $z \sim 0$, following:

$$\log \left(\frac{M_{\text{BH}}}{M_{\odot}} \right) = \alpha_1 + \beta_1 \log \left(\frac{M_{\star}}{10^{10} M_{\odot}} \right) + n(\sigma_{\text{int}}), \quad (5)$$

where α_1 is the normalization (intercept), β_1 is the slope, and σ_{int} is the intrinsic scatter in the local relation. The function $n(\sigma_{\text{int}})$ represents random Gaussian deviates centered at 0 with scale σ_{int} .

To provide a $\pm 1\sigma$ constraint on the $M_{\text{BH}}-M_{\star}$ at $z \sim 0$, we model the above line via an MCMC scheme and find

$\alpha_1 = 7.02 \pm 0.38$, $\beta_1 = 0.97 \pm 0.11$, and $\sigma_{\text{int}} = 0.37 \pm 0.05$ for the combined local sample. Figure 5 plots the local relation data and model against the WSLQs and several AGN samples at redshift $z > 0.5$ —a sample of $1 < z < 2$ AGNs from Bennert et al. (2011); one of *Chandra* X-ray-selected $0.5 < z < 1.1$ AGNs (Schramm & Silverman 2013); non-lensed AGNs at $1.2 < z < 1.7$ studied by Ding et al. (2020), henceforth denoted as D20; and several lensed AGNs (Ding et al. 2021). As with the local AGNs, we recalibrate each sample using the MgII-based M_{BH} expression in Equation (3) or the H β equation from Trakhtenbrot & Netzer (2012).

D20 find that AGN-hosting galaxies at $z \sim 1 - 1.5$ have mildly overmassive SMBHs on average for a given stellar mass, compared to the local relation. Conversely, the WSLQ sample studied here appears consistent with the local relation within roughly $\pm 1\sigma$, in line with Suh et al. (2020) who find no evolution in the $M_{\text{BH}} - M_{\star}$ relation since $z \sim 2.5$. Our updated $M_{\text{BH}} - M_{\star}$ constraints in Figure 5 do not rule out the null hypothesis of no evolution because of the intrinsic scatter in the local relation and uncertainties in the mass measurements for the previously studied AGNs.

Following recent examples in the literature (e.g., D20; Suh et al. 2020; Li et al. 2023), and to directly compare M_{BH} vs. M_{\star} as a function of cosmic time, we compute an offset from the local relation model for all AGN host galaxies in Figure 5:

$$\Delta \log \left(\frac{M_{\text{BH}}}{M_{\star}} \right) \equiv \log \left(\frac{M_{\text{BH}}}{M_{\star}} \right) - \alpha_1 - \beta_1 \log \left(\frac{M_{\star}}{10^{10} M_{\odot}} \right). \quad (6)$$

We visualize these offset values against redshift for the WSLQ systems and the other AGN samples in Figure 6. Then, we quantify the evolution in the $M_{\text{BH}} - M_{\star}$ relation with redshift by fitting a power law to the offset:

$$\Delta \log \left(\frac{M_{\text{BH}}}{M_{\star}} \right) = \gamma_M \log (1 + z), \quad (7)$$

where γ_M is the slope. Note that this form enforces the expected result of $\Delta \log (M_{\text{BH}}/M_{\star}) = 0$ at $z = 0$.

Using constraints from all samples shown in Figure 5, we find $\gamma_{M,\text{lit}} = 2.04 \pm 0.19$. Treating the WSLQs separately from the literature samples, we find $\gamma_{\text{WSLQ}} = 0.41 \pm 0.31$, suggesting a much smaller evolution – consistent with no evolution – for this subset. We quantify this discrepancy by drawing random samples from each fit’s MCMC chain and computing the percentage of instances where $\gamma_{M,\text{lit}} < \gamma_{M,\text{WSLQ}}$. This test indicates a tension of ~ 4.6 significance between the WSLQ-based model and that with the literature samples. This tension must be the result of either differences in the analyses used to deduce either of the relevant mass measure-

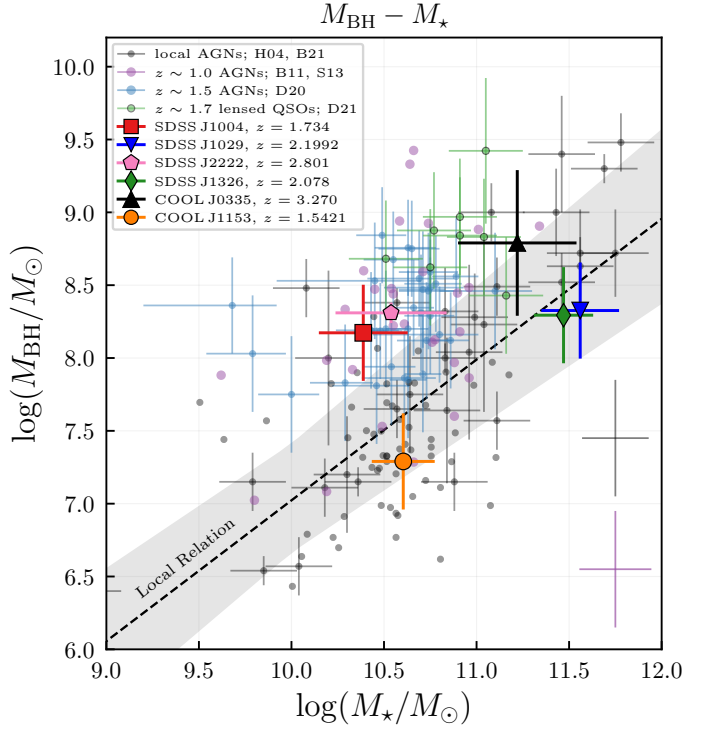


Figure 5. The WSLQ hosts plotted in $M_{\text{BH}} - M_{\star}$ parameter space against samples at other redshifts from the literature. The grey datapoints are the sample of low-redshift AGN hosts at $z < 0.1$, collated from Häring & Rix (2004) and Bennert et al. (2021). The purple datapoints are intermediate-redshift AGN hosts at $0.5 < z < 2$, with a median redshift of $z \sim 1$, from Bennert et al. (2011) and Schramm & Silverman (2013). The blue datapoints are AGN hosts from D20, at $1.2 < z < 1.7$ with a median $z \sim 1.5$, and the magenta datapoints are several lensed quasars from Ding et al. (2021). The black and purple error bars in the lower right-hand corner correspond to the uncertainties on the Bennert et al. (2021) sample and the intermediate- z AGNs, respectively. The dotted black line is the best log-linear fit to the local sample at $z < 0.1$, with the shaded grey region corresponding to the $\pm 1\sigma$ fit from the Monte Carlo chain.

ments, or reflect an underlying difference in the samples analysed here. An obvious difference is redshift—four out of six WSLQs discussed here are at $z > 2$, more distant than the vast majority of the literature samples. We explore both of these possibilities below.

4.2. Selection Effects

The intrinsic change in $\Delta \log (M_{\text{BH}}/M_{\star})$ as a function of redshift has important physical implications for the co-evolution of AGNs and galaxies, and we expect cosmological probes of AGNs to reflect that evolution. For example, a constant $\Delta \log (M_{\text{BH}}/M_{\star})$ implies that one should see a similar trend with redshift between cosmic black hole and stellar mass densities, and between cos-

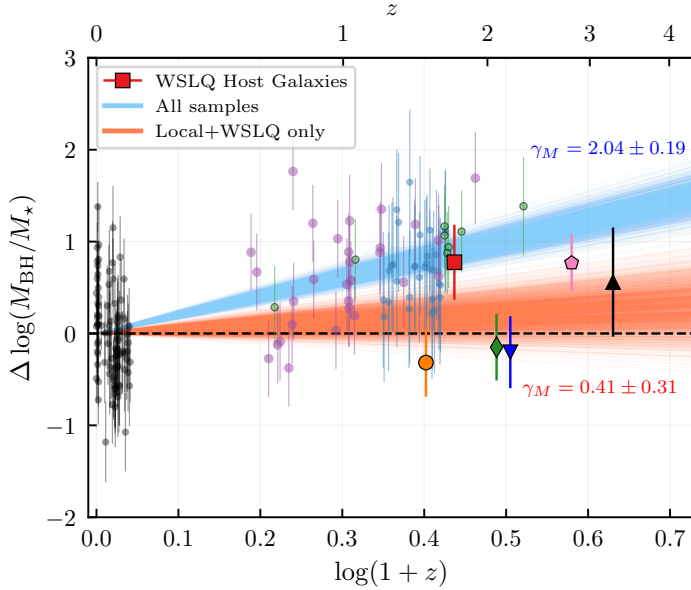


Figure 6. The offset from the measured local $M_{\text{BH}} - M_{\star}$ relation plotted against redshift for all AGN samples, as computed in Equation (6). The scattered datapoints are labeled identically as in Figure 5. The red and blue bands are random draws from the posterior of each fit, and illustrate the uncertainty. In particular, the blue band is the fit to all samples, and the red band is the fit to the WSLQs + the local AGN ‘anchor’ sample. The dotted line tracing $\Delta \log(M_{\text{BH}}/M_{\star}) = 0$ corresponds to the local-relation best-fit in Figure 5. The region between ± 0.37 on the y -axis is shaded in light grey to represent the intrinsic scatter in the local relation.

mic black hole accretion rate (BHAR) and SFR (Mulelaney et al. 2012; Suh et al. 2020).

However, we have to account for sample selection effects in order to interpret all samples in the context of AGN and galaxy populations. Following the method described later in Appendix A, for each sample at redshift $z > 0.5$ including the WSLQs, we model the selection-induced offset $\Delta \log(M_{\text{BH}}/M_{\star})$ we would expect to find if we assume that the $M_{\text{BH}} - M_{\star}$ relation does *not* evolve with redshift. After applying each offset as a bias correction to each corresponding sample, we re-fit the samples for Equation (7), one with the literature samples and the other with only the WSLQs. For the first model, we now find a power-law slope of $\gamma_{M,\text{lit}} = 1.04 \pm 0.21$, while for the WSLQ model we find $\gamma_{M,\text{WSLQ}} = -0.42 \pm 0.31$. These selection-corrected models produce a similar tension as before, of magnitude $\sim 3.9\sigma$, and we visualize the revised models and this difference in Figure 7.

While our method for subtracting out the inferred selection biases slightly reduces the tension between the WSLQ sample and the literature samples, it is still sub-

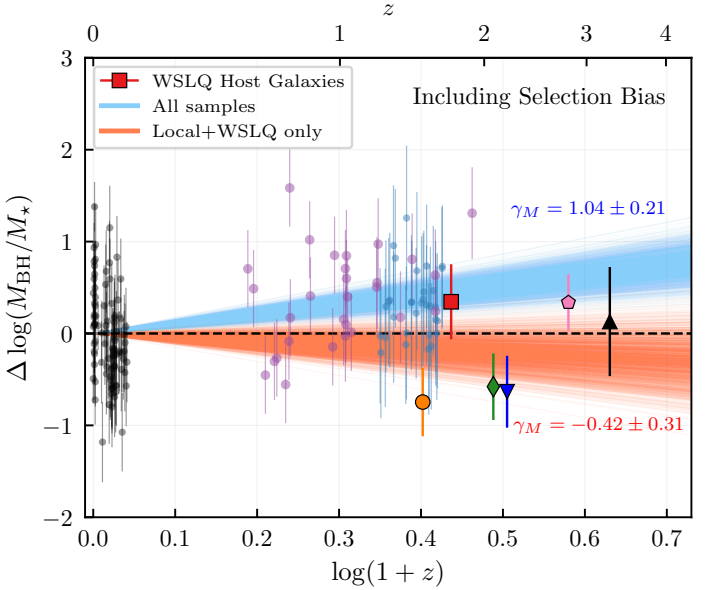


Figure 7. Identical to Figure 6, but after accounting for selection bias in the WSLQ sample and the other AGN samples at $z > 0.5$. The two models are in a similar tension as before, where the WSLQs in our sample have smaller offset values on average. Note that the sample of lensed quasars from Ding et al. (2021) is not included in this model because we do not have a selection function.

ject to further potential uncertainties and biases. X-ray observations, widely used for selection of luminous AGNs (including by D20; Bennert et al. 2011; Schramm & Silverman 2013), give a (mostly) complete census of BH accretion except for in the most obscured systems (e.g., Ricci et al. 2015). However, mildly more frequently (a factor of ~ 2), X-ray-selected AGNs reside in bluer, less massive, and more star-forming galaxies per traditional rest-UV-optical diagnostics (e.g., Aird et al. 2012), implying that X-ray samples may not be complete in M_{\star} even if they are in M_{BH} . Furthermore, radio surveys provide a more complete view of less rapidly accreting AGNs in massive galaxies, which often live in galaxy groups and are more quiescent (e.g., Best & Heckman 2012). A more complete study of selection effects in the $M_{\text{BH}} - M_{\star}$ relation will require a joint analysis using both X-ray and radio selections to minimize bias in the host galaxy population. Given that the WSLQs are classical, unobscured broad-line quasars, we assume here that they are drawn from the same quasar population at $z \sim 2$ as found in X-ray surveys.

4.3. Stellar Populations of the Hosts: SFR and M_{\star}

For each WSLQ host galaxy, in order to evaluate their location on the star formation main sequence (SFMS; e.g., Whitaker et al. 2014; Speagle et al. 2014; Leja et al.

2022; Popesso et al. 2023), we compute their SFR and specific star formation rate (sSFR) from the models in Section 3.2; these values are reported in Table 2 and plotted in Figure 8.

Note that we expect the measured SFR posterior distributions for all SED fits in our sample to be overconfident (i.e., underestimating uncertainties), given the lack of constraints on dust-obscured star formation from mid- and far-IR observations, as well as the underlying challenge of isolating unobscured AGN light contribution from the emission from stellar populations.

Considering SFRs and stellar masses for each galaxy, we note that the host galaxies of SJ1029 and SJ1326 nominally fall below the ‘star-forming main sequence’ at $z \sim 2$ (Whitaker et al. 2014). We observe these galaxies as hosting a luminous quasar, and note the possibility that these galaxies have small instantaneous SFR, and hence maybe quenched. From a purely correlative standpoint, then, these galaxies appear consistent with a scenario in which feedback from their central quasars are linked to the regulation of star forming activity.

We label the host galaxies of SJ1004, SJ2222, and CJ1153 as ‘intermediate,’ i.e., with some active star formation, where only further detailed spectroscopic followup may indicate hints of quenching or cessation of star formation.

For SJ2222, Bayliss et al. (2017) find significant Lyman- α emission within ~ 1 kpc of the accretion disk, not associated with the quasar. The authors argue that this emission is physically consistent with circumnuclear clouds (i.e., within 1 kpc of the central SMBH) that absorb outflowing UV photons in their directions before they reach star-forming regions in the host galaxy. In other words, these clouds contribute to the ‘covering factor’ of the quasar outflow (e.g., Veilleux et al. 2020, in their Sec. 3.2). Coupled with the more global presence of some star formation in the host galaxy, the physical properties of SJ2222 correlate with a scenario in which circumnuclear gas might increase the timescale of regulatory quasar feedback processes.

CJ0335 is already a massive star-forming galaxy at $z = 3.20$, and while the SFR is more uncertain than it may appear, our SFR constraints and the detected quasar activity suggests some intriguing physical hypotheses. First of all, the incidence of both the massive quasar and the SFR is consistent with the presence of dense gas in both the circumnuclear region and in the ISM. Oddly, though, the quasar is not obscured by dust since we clearly see the rest-UV quasar continuum. IR observations of this galaxy in particular would be especially interesting; strong detections would indicate that the host galaxy is a ‘luminous IR galaxy,’ and a

strong far-IR detection could mean that CJ0335 is a rare ‘cold quasar’ (Kirkpatrick et al. 2020), a blue unobscured quasar within a starburst host galaxy.

5. SYSTEMATICS AND LIMITATIONS

As already noted in Section 4, deducing evolutionary trends from a redshift-ordered set of incomplete cross-sectional samples is a potentially fraught process. Numerous potential systematics, some specific to individual samples, and others more broadly applicable, should be considered. Specifically, strongly lensed sources may have biases related to lens modeling. All of the samples discussed here will have biases from the SED fitting treatment of heterogeneous data, influencing the resulting M_* and SFR measurements. The choice of comparison samples must also be considered. The potential systematics and the limitations they impose are considered below.

5.1. Uncertainties in Lensing Magnifications

As lens modeling quantifies the degree to which lensed sources are magnified, accurate and precise lens models are crucial in order to transform observed properties of lensed sources to their intrinsic, unlensed values. To investigate lens modeling systematics, we recompute M_{BH} and M_* for each WSLQ system (except for SJ2222) after perturbing the magnification μ_m by each of $\pm 1\sigma$, a factor of 1/2, and a factor of 2. The motivation for this test is twofold. One idea is that the perturbed mass measurements give a more complete view of the statistical uncertainties in M_{BH} and M_* . The other is that it provides a consistency check of our methodology. If both M_* and M_{BH} depend on the lensing magnification, then perturbing the magnification should simply shift a lensed quasar’s location in $M_{\text{BH}} - M_*$ parameter space in a direction roughly parallel to the local relation.

As shown in Figure 9, each WSLQ’s position in $M_{\text{BH}} - M_*$ parameter space relative to the local relation does not change significantly as we perturb the magnification. We therefore conclude the perturbed measurements do remain consistent with our results for the $M_{\text{BH}} - M_*$ relation in Section 4. Note, though, that an underestimated magnification would result in a slightly overestimated offset $\Delta \log(M_{\text{BH}}/M_*)$ and vice versa. This trend stems from how the perturbation impacts M_* and M_{BH} . While M_* scales linearly with μ_m , M_{BH} does not, according to Equation (3). Instead, L_{3000} scales linearly with μ_m , and so M_{BH} scales as $\mu^{0.62}$.

We must mention that a notable degree of magnification uncertainty does exist in the present archival data of WSLQs, even with the resolution of *HST*. Such is especially the case for SJ1326, CJ0335, and CJ1153, for

Name	μ_m	Line	$\log(\lambda L_\lambda)$	ΔV (km s $^{-1}$)	$\log(M_{\text{BH}}/M_\odot)$	$\log(M_*/M_\odot)$	$\log(\text{SFR}/M_\odot \text{ yr}^{-1})$	$\log(\text{sSFR}/\text{yr}^{-1})$
SJ1004	23.3 ± 7.2	MgII	44.00	2690	8.17 ± 0.33	$10.39^{+0.14}_{-0.24}$	$1.31^{+0.30}_{-0.83}$	$-8.94^{+0.36}_{-0.41}$
SJ1029	5.5 ± 0.3	MgII	45.08	2554	8.35 ± 0.33	$11.56^{+0.14}_{-0.21}$	$0.38^{+0.40}_{-0.20}$	$-11.34^{+0.43}_{-0.20}$
SJ2222	12.0 ± 5.0	$8.31 \pm 0.07^{\text{a}}$	$10.54^{+0.24}_{-0.30}$	$1.67^{+0.36}_{-0.52}$	$-9.08^{+0.65}_{-0.49}$
SJ1326	3.0^{+2}_{-1}	MgII	44.52	3913	8.29 ± 0.33	$11.47^{+0.15}_{-0.10}$	$1.19^{+0.46}_{-0.18}$	$-10.45^{+0.59}_{-0.16}$
CJ0335	$5.3^{+3.4}_{-1.8}$	CIV	44.15	10017	8.79 ± 0.5	$11.22^{+0.31}_{-0.37}$	$2.74^{+0.19}_{-0.12}$	$-8.62^{+0.43}_{-0.35}$
CJ1153	5.2 ± 0.6	MgII	43.44	2774.6	7.29 ± 0.33	$10.60^{+0.12}_{-0.17}$	$0.40^{+1.09}_{-1.16}$	$-10.37^{+1.15}_{-1.10}$

^a from Williams et al. (2021b)

Table 2. Source-plane quasar and host galaxy properties for the WSLQs studied in this work. Magnification values, used to transform measurements into the source plane are given in the second column, and they correspond to the green-circled images in Figure 1. Columns from left to right: WSLQ name, magnification, broad emission line of choice for modeling M_{BH} , quasar continuum luminosity in erg s $^{-1}$, broad-line FWHM in km s $^{-1}$, SMBH mass, host stellar mass, host SFR, and host specific SFR. The sSFR is computed as $\text{SFR}/M_{*,\text{tot}}$. Note that for CJ0335, the FWHM reported has been corrected according to the measured centroid blueshift in CIV emission, as outlined in the text.

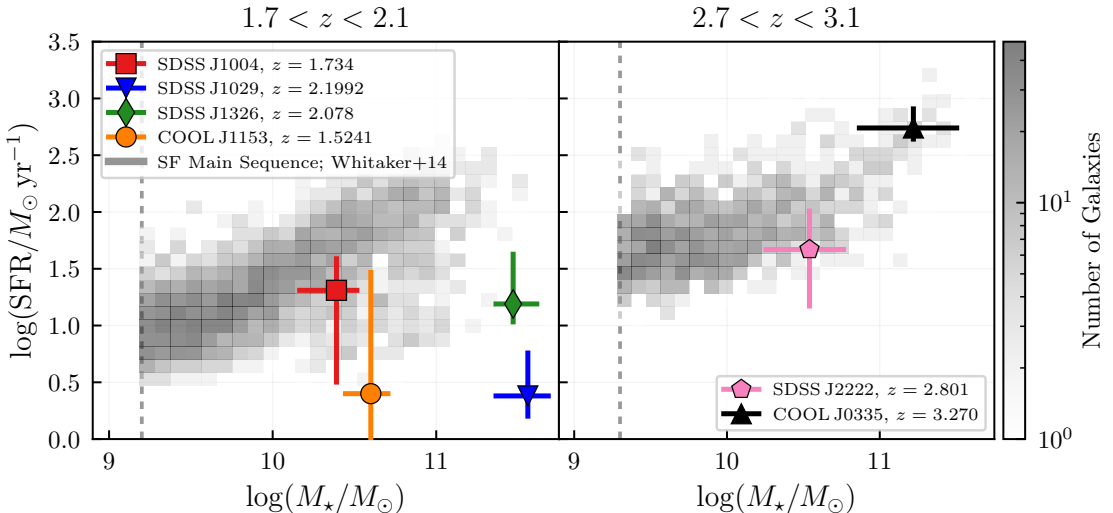


Figure 8. The WSLQ host galaxies plotted over the star-forming main sequence at respective redshifts, measured with *HST* and *Spitzer* photometry by Whitaker et al. (2014), from which the grey meshplots come. SJ1029 and SJ1326 fall below the main sequence, implying that they have already quenched or are in the process of quenching at the observed epoch. The SFR distribution for CJ1153 is mostly below the main sequence but is still consistent within $+1 - 2\sigma$, leaving the interpretation more uncertain. SJ1004 and SJ2222 appear similarly consistent with lying on the main sequence but seem more likely to sit just below it. CJ0335 sits on the main sequence, appearing consistent with being a massive star-forming galaxy.

which only ground-based imaging exists. A more careful analysis of each WSLQ’s lens model, using better imaging data, is required to fully unpack the lens modeling systematics. This level of detail is beyond the scope of this work. At the same time, from our analysis, uncertainties in the magnification do not appear to significantly impact the results.

5.1.1. Multiple Quasar Images

In this work, we have so far analyzed one lensed image for each WSLQ system. If the methodology is robust and the measurements are accurate, then we ought to find the same results for a given quasar and host galaxy

using different lensed images. To test that idea and further verify our methods, we measure and compare M_{BH} , M_* , and other host galaxy properties between the three brightest images for two WSLQ systems: SJ1004 and CJ1153.

For SJ1004 and CJ1153, we replicate each target’s respective analysis for each image as in Section 3, with some key differences to ensure self-consistency. In particular, our methods for obtaining image-plane photometry and for SED modeling are unchanged for each. For SJ1004 we remagnify and then demagnify archival photometric measurements from Ross et al. (2009), who re-

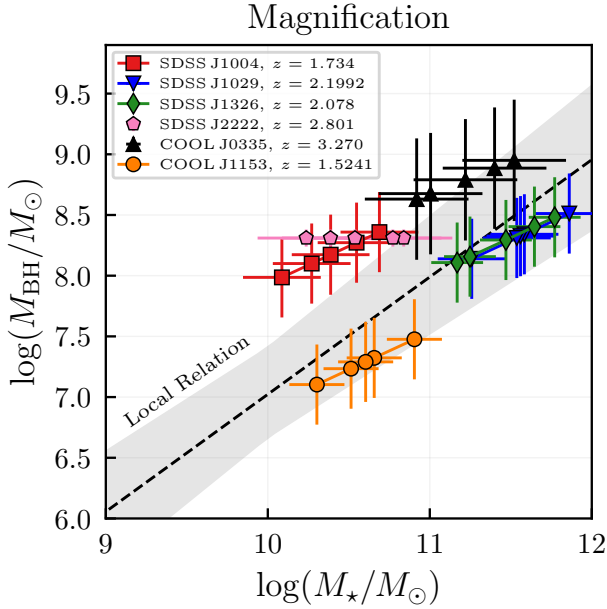


Figure 9. Similar to Figure 5, but now with μ_m -perturbed measurements of M_{BH} and M_{\star} . The magnifications shown in an array are $(\mu_m/2, \mu_m - 1\sigma, \mu_m, \mu_m + 1\sigma, 2\mu_m)$. Other samples shown in Figure 5 are removed for the sake of visual clarity. Note that SJ2222 is not perturbed in M_{BH} because the reverberation mapping measurement is independent of magnification.

port host galaxy fluxes for its three brightest images. For CJ1153 we perform SB modeling of images B and C using GALFIT to extract host galaxy magnitudes, as in Section 3.1.

Regarding M_{BH} and spectroscopy, for SJ1004, the eBOSS programs obtained a spectrum of image B as well as image A, but not of image C. To approximate a MgII emission line of SJ1004's image C, we compute a flux ratio between images A and C in the z -band using the fluxes from the public DECaLS DR10 catalog. We then rescale the spectrum of image A by that ratio and repeat the spectroscopic analysis outlined in Section 3.3. We repeat this rescaling to estimate M_{BH} for images B and C of CJ1153.

We have implicitly assumed that the difference between the magnification of the quasar and that of its host is negligible. As a simple test for the assumption that there is no difference, for SJ1004 and CJ1153, we compute the average magnification of the host as follows. We draw a contour around the host flux in the image plane, compute the corresponding ‘undeflected’ contour in the source plane, and then compute the image-to-source ratio of projected areas as the magnification. The statistical 1σ uncertainties are derived by repeating the process with 100 iterations of the lens model, randomly

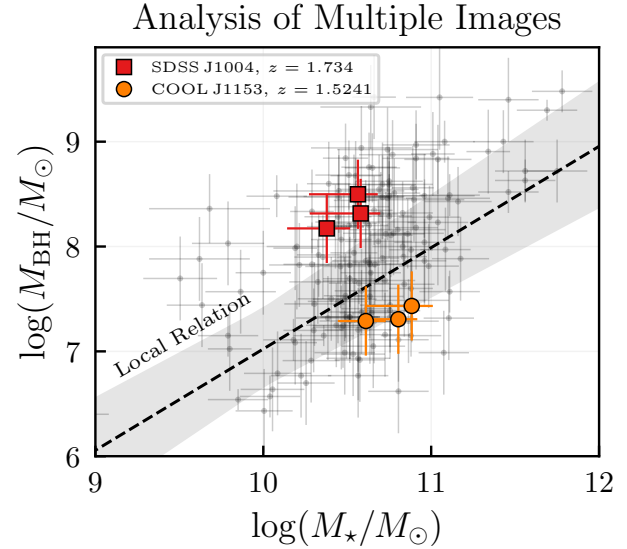


Figure 10. A nearly identical plot as Figure 9, instead comparing M_{BH} and M_{\star} of different quasar images for SJ1004, CJ0335, and CJ1153. All of the samples from the literature are plotted as grey datapoints, and the local relation is the grey band.

drawn from the MCMC posterior. Then, we rescale the photometry of each host galaxy image by its average magnification and recalculate M_{\star} and other host galaxy properties. As a test for lensing and magnification systematics, note that our methods are not comprehensive, as other issues can easily arise such as magnification gradients, which may require greater attention to detail than this test gives (e.g., Klein et al. 2024).

M_{\star} and M_{BH} derived from the multiple images of each system are shown in Figure 10. For both SJ1004 and CJ1153, their three images appear consistent with one another within $\sim 1\sigma$, and the principal axis of dispersion appears to be visually similar to that traced by the perturbations in Figure 9. In addition, the three WSLQs remain consistent with what we find in Section 4.1. This test for consistency between images implies that systematics related to lensing configurations, or differences between images, do not significantly influence our primary results in Section 3. Furthermore, this check also indicates that quasar variability is not an important issue either, since each image is captured at a different time along the light-curve due to time-delays (Fohlmeister et al. 2013; Dahle et al. 2015; Muñoz et al. 2022; Napier et al. 2023a).

We list the different measurements of μ_m , M_{\star} , and M_{BH} for each image in Table 3.

5.2. Stellar Population Synthesis Systematics

Image	$\mu_{\text{m,QSO}}$	$\mu_{\text{m,host}}$	$\log(M_{\text{BH}}/M_{\odot})$	$\log(M_{\star}/M_{\odot})$
SJ1004-A	$23.3^{+7.2}_{-7.2}$	$23.7^{+6.0}_{-5.1}$	8.17 ± 0.33	$10.38^{+0.14}_{-0.24}$
SJ1004-B	$13.8^{+3.8}_{-3.8}$	$15.6^{+3.6}_{-2.9}$	8.50 ± 0.33	$10.56^{+0.12}_{-0.29}$
SJ1004-C	$10.7^{+1.3}_{-1.3}$	$11.0^{+1.3}_{-1.3}$	8.32 ± 0.33	$10.58^{+0.12}_{-0.30}$
CJ1153-A	$5.2^{+0.6}_{-0.6}$	$5.1^{+0.7}_{-0.5}$	7.29 ± 0.33	$10.61^{+0.12}_{-0.17}$
CJ1153-B	$3.9^{+1.8}_{-1.2}$	$5.3^{+2.1}_{-1.6}$	7.43 ± 0.33	$10.88^{+0.13}_{-0.27}$
CJ1153-C	$5.3^{+0.9}_{-0.9}$	$5.3^{+0.9}_{-0.9}$	7.31 ± 0.33	$10.80^{+0.12}_{-0.23}$

Table 3. Properties from analysis of multiple lensed images. The columns are as follows, from left to right: the quasar image, magnification as computed from a contour around quasar flux, magnification for a contour around host galaxy flux, black hole mass, and stellar mass. The magnifications of the host and quasar are consistent within 1σ for each quasar image.

5.2.1. Intrinsic M_{\star} Offsets from SPS Models

Constraining a galaxy’s SFH is a nontrivial exercise. The associated parameter space is highly nonlinear, and nearly all SED models will need to make some simplifying assumptions in order to extract useful information (Conroy 2013; Carnall et al. 2019). Various biases associated with SFH model choices will infiltrate into the results, and any robust study of galaxy SEDs and derived properties ought to account for these biases. To that end, we explore the impact of assuming the delayed-tau model on our M_{\star} measurements. To do so, we take a random sample of 311 well-studied galaxies from the CANDELS field (Santini et al. 2015) at $0.5 < z < 5$. We fit each galaxy with a simple version of the SPS framework from Section 3.2, with $M_{\star,\text{tot}}$, t_{age} , τ , and $\tau_{\lambda,2}$ as free parameters, and without continuum or emission from interstellar nebulae or dust.

We compare model results on CANDELS galaxies to the previous M_{\star} measurements from Santini et al. (2015) in order to probe intrinsic bias in the stellar mass constraints for WLSQ host galaxies. As shown in Figure 11, we compute the difference between the catalog M_{\star} values and the new values and measure the (residual) difference as a function of catalog redshift z_{best} . Similarly to how we constrain the time-evolution of $\Delta \log(M_{\text{BH}}/M_{\star})$, we fit a power law (a logarithmic slope and intercept) with an MCMC code to characterize how the residual changes with redshift. Given the uncertainty shown on the power-law model and the distribution of datapoints at $z < 1.5$ slightly below 0, and specifically assuming that the measurements from Santini et al. (2015) are accurate, the SPS modeling framework used here might overestimate M_{\star} on average by ~ 0.1 dex at low redshift. More broadly, we suggest that uncertainties at this level should be taken as a bare

minimum uncertainty (Lower et al. 2020) in the comparison between various literature quasar samples used here, each of which have their own SPS treatment.

5.2.2. SPS Model Choices and Heterogeneity in Individual WSLQ Hosts

In Section 3.2, we adjusted the SPS model of a given WSLQ host galaxy based on the constraining power of available photometry. To test for biases from this heterogeneity, we adopt a simpler model setup and a more complex, more flexible setup and apply each of these to the host galaxies of SJ1029 and SJ1326. We choose these two hosts because they are least well-constrained by the available photometry with only three measurements each (Table 1).

Here, for dust attenuation, instead of Calzetti et al. (2000), we use the formalism of Kriek & Conroy (2013) which uses two additional dust parameters. These are (a) the attenuation around young stellar populations and (b) the slope of the attenuation curve. The motivation for using this attenuation curve is that it is likely more suitable for distant galaxies. The simpler model keeps $M_{\star,\text{tot}}$, t_{age} , τ , and attenuation around older stellar populations as free parameters and keeps stellar metallicity constant, while setting the two attenuations (older and younger) to be equal. The more complex model is similar to the model for SJ1004 in Section 3.2, while adding attenuation around young stars and the attenuation slope via the Kriek & Conroy (2013) curve. For SJ1029, the more complex model again contains a suspicious dusty solution that is likely too massive and star-forming at the same time; we again rule out this solution.

We find that the host galaxy parameters of SJ1029 and SJ1326 are affected strongly by the model heterogeneity. The simpler model for SJ1029 gives results which are consistent with the model from Section 3.2, but the more flexible model gives a SFR posterior which is larger than before at a rate of $\sim 1.4\sigma$ even excluding the suspicious solution. We find a similar result with SJ1326, where the simpler model is more consistent but the flexible model gives a larger SFR by $\sim 1.2\sigma$. Figure 12 visualizes these differences in SFR measurements for both galaxies, alongside the stellar masses and SEDs for the corresponding models.

Comparing the simple and flexible models directly, the inferred median stellar mass is less sensitive to the model choice, but the scatter in the distribution may change as it does for SJ1326. The SFR is much more sensitive, to the extent that it can change where a galaxy falls in the M_{\star} –SFR plot (star-forming, quiescent, or starburst). While not consequential in every case, this outcome validates our expectation that SPS model choices influence

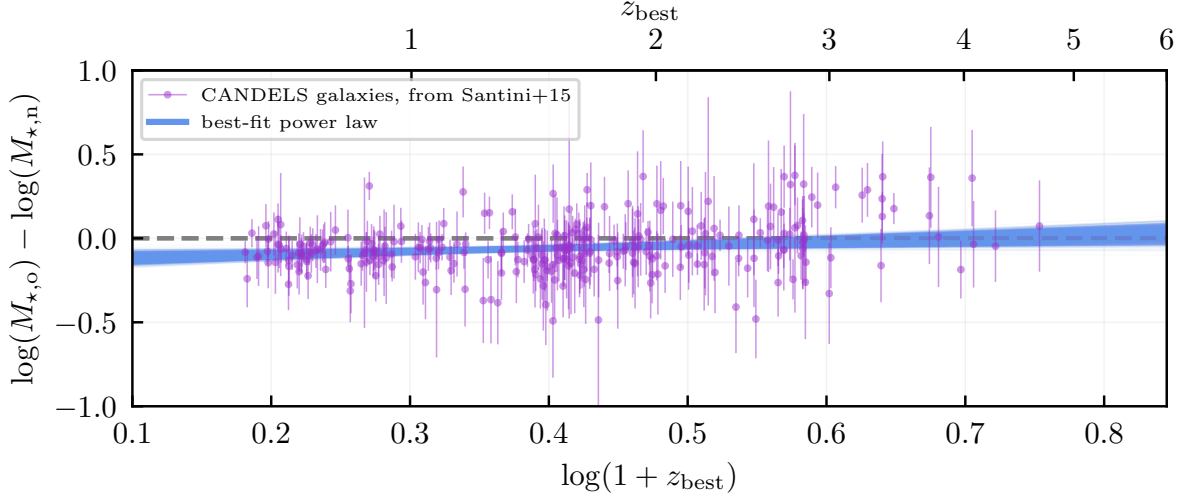


Figure 11. Residual between the Santini et al. (2015) measurements $M_{*,o}$ and our measurements $M_{*,n}$ for CANDELS galaxies as a function of redshift. The blue band is a random sample of power-law fits computed using an MCMC scheme. We do not find significant offsets of concern, while noting that the SPS framework we employ may slightly overestimate M_* on average at lower redshift.

the model results and the corresponding interpretations. Furthermore, it indicates that the actual physical uncertainties in SFR are larger than the statistical ones given by the model, as we discussed in Section 4.3. Follow-up IR observations and/or much deeper spectroscopy would be required to better constrain the host galaxy SEDs and their star formation histories.

On a more specific note about SJ1029, the host galaxy has been observed with *Herschel Space Observatory*, as Stacey et al. (2018) detected flux at each of 250, 350, and 500 μm (see their Table A1), indicating a presence of thermal emission from cold dust. In addition to a desire to preserve what homogeneity exists in the WSLQ sample, we elect not to include this far-IR photometry in the fiducial SPS model for SJ1029 for two reasons. (1) If we add it and remove the upper limit on $\tau_{\lambda,2}$, we find that M_* and SFR are not significantly impacted. The corresponding dust constraint of $\tau_{\lambda,2} = 0.94^{+0.20}_{-0.10}$ does challenge the specific choice of $\tau_{\lambda,2} < 1$ from Section 3.2, but it does not change our interpretations of SJ1029 in the $M_{\text{BH}}-M_*$ relation or its stellar populations. The host galaxy is massive and it probably contains a small but notable amount of dust (given the faint far-IR detection), and its SFR is not well constrained. (2) For sufficiently dusty clouds in a quasar host galaxy, the traditional assumption that cold dust emission is powered by star formation may break down (McKinney et al. 2021). If the quasar produces at least some of the far-IR, then a model including *Herschel* photometry would overestimate the host galaxy IR emission. We cannot confirm that the host galaxy is driving this far-IR emission in

full, and including it here would make that assumption and therefore potentially bias the model posteriors.

The choice of stellar population model affects measurements both of WSLQs from this work and of AGNs from the literature. For example, D20 use simple stellar population templates of specific ages fit to the host galaxy photometry to constrain M_* . They use the 21/32 host galaxies with robust photometric detections in two HST filters (either F140W or F125W, plus F814W) to choose a single template age for two redshift subsamples of $1.23 < z < 1.44$ and $1.44 < z < 1.67$. D20 then apply these same templates to the 11/32 systems which have no detection in the bluer filter (F814W), anchoring their results for these systems only on the NIR single-band photometry. Given the demonstrated range of host galaxy properties and colors—seen here and in extensive literature (e.g., Dunlop et al. 2003; Simmons et al. 2012; Glikman et al. 2015; Ding et al. 2022)—it seems equally plausible that this 1/3rd of their sample are instead actually older and redder host galaxies, whose masses will not be well measured by matching to a younger template.

Potentially, this measurement bias in M_* could account for some of the observed difference between the fits to the different samples in Section 4.1; further data able to better constrain the stellar populations in these galaxies would be required to suppress this potential bias. Note that if we remove the D20 sample altogether, then we instead get a fit described by $\gamma_{M,\text{lit}} = 1.22 \pm 0.28$, which still differs from the WSLQ fit by $\sim 4.0\sigma$.

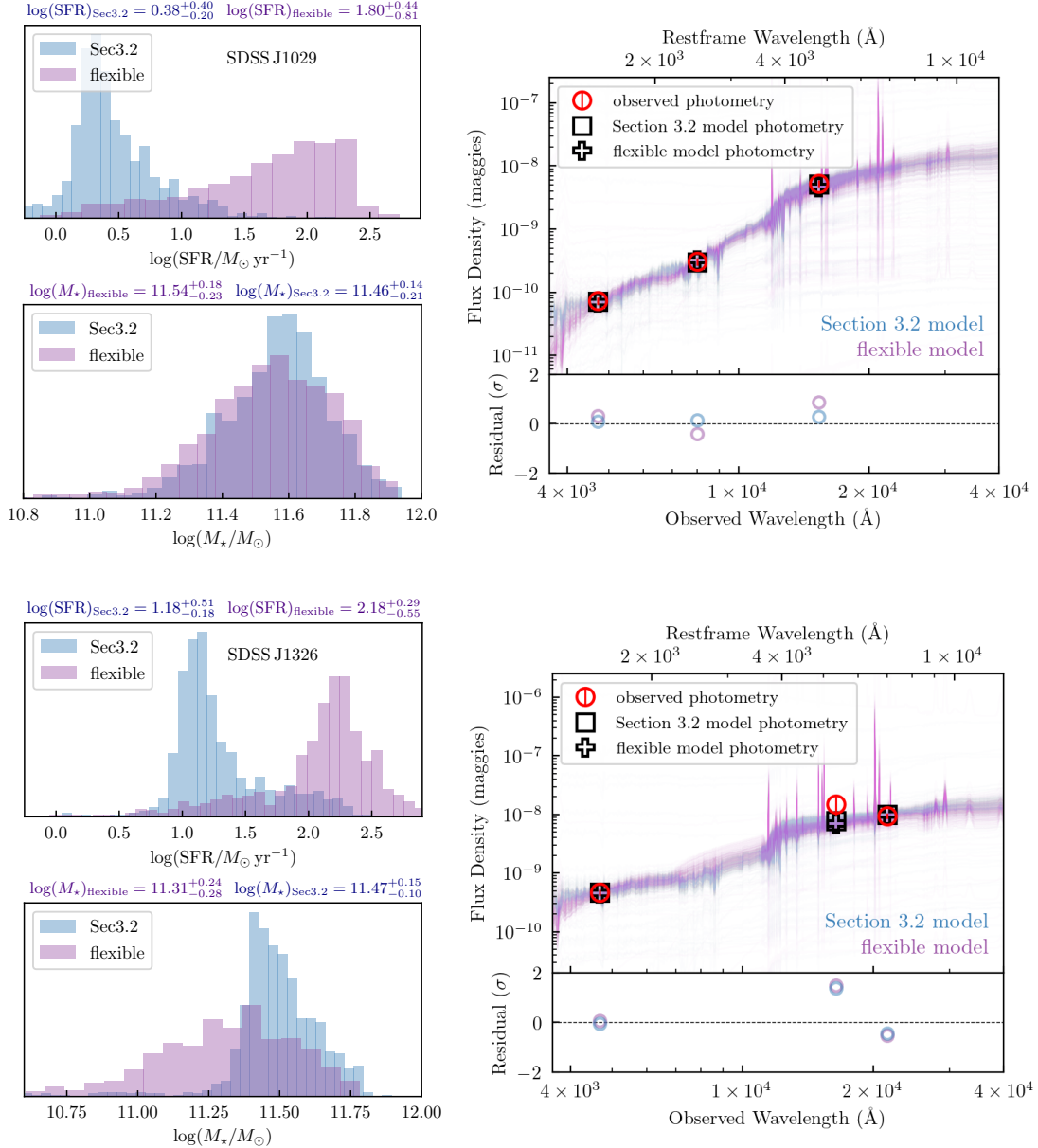


Figure 12. Comparison of output galaxy SEDs, M_* distributions, and SFR distributions between the models described in Section 3.2 and the more flexible models, for the host galaxies of SJ1029 (top) and SJ1326 (bottom). Models from before are shown in light blue, while the more flexible uniform models are shown in purple/magenta. While the SED fits are similar from a statistical, least-squares perspective, the SFR constraints differ between the two models by $\gtrsim 1\sigma$ for both galaxies.

In addition, note that two of the known eight WSLQs were not included in the analysis presented here, as no detection of the host galaxy was apparent in the extant data. Notably, at the time of writing, the available data on both of these systems was only ground-based imaging of moderate seeing and depth, and so the lack of a host-galaxy detection may simply reflect the limits of available data. However, it is possible that these two systems have preferentially larger $\Delta \log(M_{\text{BH}}/M_*)$ val-

ues, further lessening the few-sigma tension between the WSLQ results and other data.

5.3. The Local Anchor and Self-Consistency

The choice of local sample used in ‘anchoring’ higher redshift AGN samples can bias the resulting analysis of how galaxies and SMBHs co-evolve (e.g., Bennert et al. 2021; Li et al. 2023). To minimize this bias, a common solution is to use samples from the literature not only which are relatively complete (Appendix A), but also to

which the authors can easily apply their own methods (i.e., ‘self-consistency’). In other words, when choosing a local anchor, we ought to collate samples for which techniques as similar to ours as possible are used for M_{BH} and M_{\star} measurements. In line with this idea, we have used the local sample from [Bennert et al. \(2021\)](#), who use single-epoch spectroscopy for M_{BH} and photometry and color information for M_{\star} (albeit using a different code and set of templates for SED fitting). Furthermore, the [Bennert et al. \(2021\)](#) local AGN sample is relatively diverse in terms of host galaxy morphology. However, taken alone the [Bennert et al. \(2021\)](#) sample poorly constrains the slope of the local relation. Hence, following D20, in the above we supplemented this dataset with a nearby sample of massive quiescent galaxies from [Häring & Rix \(2004\)](#), many of whose SMBHs are not actively accreting but which extends to higher M_{BH} and thus better constrains the model of the local relation in Section 4.1. Stellar masses for these systems are an aggregate of various detailed analyses from the literature, but the sample itself is almost exclusively early-type galaxies. Given differences in methodology and host-galaxy populations between [Häring & Rix \(2004\)](#) and [Bennert et al. \(2021\)](#), and the higher-redshift comparisons, we may expect some systematic biases in stellar masses in our measurement of the $M_{\text{BH}}-M_{\star}$.

Self-consistency in M_{BH} measurements is often more important and consequential, due to the larger uncertainty (sans reverberation mapping) and the wider variety of calibrations and different recipes ([Trakhtenbrot & Netzer 2012](#); [Ding et al. 2020](#)). As such, for comparison to WSLQs, we have selected samples from other papers ([Bennert et al. 2011](#); [Schramm & Silverman 2013](#); [Ding et al. 2020](#); [Ding et al. 2021](#)) which use single-epoch spectroscopic measurements of either MgII or a Balmer line ($\text{H}\beta$, $\text{H}\alpha$). We recalibrated M_{BH} values from other papers in the analysis of the $M_{\text{BH}}-M_{\star}$ relation where possible.

However, even with self-consistency in M_{BH} maximized, there are multiple MgII-based calibrations of M_{BH} in the literature and the choice of which to use impacts the results of the fits detailed in Section 4. If, rather than the formalism from [Trakhtenbrot & Netzer \(2012\)](#), we instead adopt the recipe given by [Ding et al. \(2021\)](#) in their Section 2, we find a similar slope and intrinsic scatter but a higher normalization in the local relation by ~ 0.3 dex (i.e., the local relation shifts upward). For the fit to the literature AGN samples, this change results in a best-fit offset $\Delta \log(M_{\text{BH}}/M_{\star})$ which is consistent at $< 1\sigma$ with no $M_{\text{BH}}-M_{\star}$ evolution, with $\gamma_{M,\text{lit}} = 0.25 \pm 0.27$ instead of $\gamma_{M,\text{lit}} = 1.04 \pm 0.21$ after accounting for selection effects. For the WSLQ-

only fit, we find $\gamma_{M,\text{WSLQ}} = -0.77 \pm 0.33$ instead of $\gamma_{M,\text{WSLQ}} = -0.42 \pm 0.31$; i.e., a mild tension between the WSLQ measurement and that from other samples remains, but the overall picture is more consistent with no evolution. Broadly, this is consistent with the models of [Yang et al. \(2018\)](#), [Shankar et al. \(2020\)](#), and [Tanaka et al. \(2024\)](#), whose results each span no evolution to mildly positive evolution in the $M_{\text{BH}}-M_{\star}$ relation since $z \sim 2$. In other words, by that cosmic epoch the local $M_{\text{BH}}-M_{\star}$ relation has mostly been established.

6. DISCUSSION

In formulating the black hole accretion rate (BHAR) as a function of galaxy stellar mass and redshift, with M_{BH}/M_{\star} at $z = 4$ as an ‘initial’ condition, [Yang et al. \(2018\)](#) infer a weak redshift evolution in the time-averaged ratio between BHAR and SFR from $z \sim 3$ to $z \sim 0.8$. This result corresponds to weak evolution (if any) in the $M_{\text{BH}}-M_{\star}$ relation over that time. As both the BHAR and SFR densities are much lower at $z \lesssim 0.8$ than at $z \gtrsim 2$, the authors assume that both are essentially negligible after $z \sim 0.8$, and therefore the local $M_{\text{BH}}-M_{\star}$ relation has nearly been established by $z \sim 2$.

The full selection-corrected fit (including WSLQs, samples from the literature, and considering selection biases) discussed in detail above exhibits at most only mild evolution in M_{BH}/M_{\star} since $z \sim 2$. This interpretation is more of an upper limit, as the fitted index of the power-law evolution in redshift $\gamma_{M,\text{lit}} = 1.04 \pm 0.21$ gives offsets of similar magnitude to the intrinsic scatter of the local relation at $z = 0$. Therefore, the fit to the literature data ($\gamma_{M,\text{lit}}$) appears consistent with [Yang et al. \(2018\)](#). The WSLQ-only model ($\gamma_{M,\text{WSLQ}}$) is consistent with no evolution, at $\sim 1.2\sigma$ below $\Delta \log(M_{\text{BH}}/M_{\star}) = 0$ before including intrinsic scatter σ_{int} .

Moreover, we remind the reader that the redshift power-law evolution explored in prior papers and used here is almost certainly not an adequate description of the complex evolution of AGNs and their host galaxies over the entirety of cosmic time, and that the construction of an evolutionary sequence from time-ordered, cross-sectional samples selected and studied in various ways is a challenging process, at best.

Recently, early observational works with *JWST* have found a much larger $\Delta \log(M_{\text{BH}}/M_{\star})$ in the early universe ($z \gtrsim 5$) (e.g. [Maiolino et al. 2023](#); [Puccetti et al. 2023](#); [Stone et al. 2023](#)), though whether that detection is intrinsic or merely a product of selection bias is not yet clear ([Li et al. 2024](#)). If real, this larger $\Delta \log(M_{\text{BH}}/M_{\star})$ at early times would support more rapid cosmic SMBH growth at high redshift and/or ‘heavy’ SMBH seeding (e.g., [Schneider et al. 2023](#)), followed by starburst activ-

ity such that M_* ‘catches up’ by a later time. In that context, the small time evolution in $\Delta \log(M_{\text{BH}}/M_*)$ since $z \sim 2$ shown by the literature samples in Figure 7 would represent an intermediate point between very early and late times, by which M_* has mostly but not entirely caught up.

Both a larger average offset at higher redshift $z \gtrsim 5$ and that of a negligible offset at that time remain open possibilities. The WSLQ-only fit on its own is more consistent with a smaller offset (i.e., less rapid accretion and/or a different SMBH seeding scenario) at early times, and informs a redshift interval ($2 < z < 3$) where there are at present few other constraints. Interestingly, assuming our measurements are accurate and that the fit to the literature data is closer to the ‘true’ evolution, the WSLQs’ smaller $\Delta \log(M_{\text{BH}}/M_*)$ values imply that they would fall on either the negative tail of the BHAR distribution function or the positive tail of the SFR distribution function (each time-averaged; Yang et al. 2018) for galaxies hosting unobscured broad-line quasars.

Regardless, these results clearly highlight the need for more detailed, *multi-wavelength* reconstructions of AGN-fueled outflows, star formation histories, and conditions of the interstellar media in tandem and in greater detail at higher redshift. Spatially cross-correlating physical imprints of AGN activity with interstellar gas physics and star formation could illuminate the role(s) of AGNs in galaxy evolution and star formation in much more detail. Considering the level of precision in our measurements of WSLQs using relatively unexceptional (i.e., not groundbreaking) data quality, we emphasize that WSLQs and other highly magnified AGNs are among the most intriguing targets for these types of detailed study at any redshift they can be discovered (e.g., Furtak et al. 2023).

7. SUMMARY

With the available archival data and new observations obtained by the COOL-LAMPS collaboration, we use a sample of six unobscured broad-line quasars strongly lensed by massive galaxy clusters in order to study the $M_{\text{BH}}-M_*$ relation and the co-evolution of SMBHs and galaxies from $z \sim 3$ to $z = 0$. These ‘wide-separation lensed quasars’ are among the most highly magnified multiply-imaged quasars known. More specifically, we constrain quasar host galaxy properties (stellar mass and star formation rates, primarily) via the stellar population synthesis code **Prospector**. We constrain the quasar black hole masses by modeling the flux profile of a chosen rest-UV broad emission line, observed with single-epoch spectroscopy. These physical properties provide constraints on the time evolution of the

$M_{\text{BH}}-M_*$ relation. In cases where the analysis is possible, we analyze multiple images of a given quasar, and demonstrate good agreement in results from these different images.

We model potential evolution in the $M_{\text{BH}}-M_*$ relation from $z \sim 0$ as a power law with a normalization coefficient and a parameter for intrinsic scatter. We consider two fits describing the time evolution in $M_{\text{BH}}-M_*$, parametrized by $\Delta \log(M_{\text{BH}}/M_*)$ in Equation (6): one fit to a set of other mostly unlensed samples at different—and mostly lower—redshifts, and one fit to only the WSLQs and a local AGN sample.

The primary conclusions in this paper are as follows:

- Highly magnified AGNs are among the most intriguing individual systems for future detailed study of AGN outflows, feedback, and the physical relation(s) therein to galaxy evolution. Even when relying on ground-based imaging, we have in some cases confidently detected each WSLQ’s host galaxy flux and placed strong constraints on the stellar mass. This outcome is remarkable and possibly unique to WSLQs among luminous broad-line quasars; at cosmological distances, much higher resolution data from over-subscribed observatories such as *HST*, ALMA, or *JWST* is usually required to at all constrain host galaxy masses, luminosities, and other properties (e.g., Peng et al. 2006; Li et al. 2023; Tanaka et al. 2024). Pairing such observations with the advantages of cluster-scale lensing could give further powerful constraints on AGN–host co-evolution and feedback at high redshift, particularly with the expanded samples expected from the Rubin Observatory (Napier et al. 2023a).
- The WSLQs are consistent with the local $M_{\text{BH}}-M_*$ relation and therefore with a scenario in which M_{BH}/M_* is relatively constant since $z \sim 3$. This result contrasts with a fit to some AGN samples from the literature, with which the fit to the WSLQ sample differs by 4σ .
- The WSLQ hosts are a mixture of star-forming and quiescent galaxy candidates. SJ1029 and SJ1326 are quiescent galaxy candidates, as some models of their stellar populations give SFRs which fall below the star-forming ‘main sequence.’ SJ1004, SJ2222, and CJ1153 have less constrained SFRs, given the existing data fit with a wide range of SPS models. CJ0335 is most consistent with a massive star-forming galaxy, despite the quasar’s unobscured nature—we hypothesize that if the host galaxy is strongly detected in the far-IR,

then it may be a rare ‘cold quasar’ in addition to an absorption-line quasar (Kirkpatrick et al. 2020; Napier et al. 2023b). Currently available data is insufficient to robustly confirm or rule out scenarios for these host galaxy stellar populations. As such we avoid definitive statements on star formation histories, for which stronger constraints would require follow-up multi-wavelength observations. Whether individual WSLQ host galaxies are star-forming or quiescent, they represent intriguing future case studies for AGN feedback, as different types of stellar populations may represent various co-evolutionary stages between SMBHs and galaxies (Hopkins et al. 2006).

- We investigate several sources of systematic uncertainty and make a number of simple tests, to verify or further explore the results for WSLQ host galaxy properties and the $M_{\text{BH}} - M_{\star}$ relation. Potentially significant systematic issues include: selection bias (Section 4.2, Appendix A), the SPS modeling framework (Section 5.2), and the choice of local anchor or of M_{BH} calibration (Section 5.3). Additionally we explore the impact of uncertain magnifications and of the choice between different lensed images (Section 5.1) The selection effects and the local anchor are both important, but none of the other choices significantly affect our interpretations.

Upcoming wide-area surveys (*Euclid*, LSST, *Roman*) will drastically increase the discovery space and should grow the sample size of strongly lensed AGNs, including WSLQs. Additionally, the recent developments in IR observations make possible a number of strong potential improvements to our results and directions for additional study. *JWST* imaging at NIR and mid-IR wavelengths would significantly improve the lens modeling (Napier et al. 2023a), but it would also greatly facilitate bulge–disk decomposition to study the $M_{\text{BH}} - M_{\star, \text{bulge}}$ relation. We can employ IR spectroscopy for a number of purposes, including: (1) improvements in the M_{BH} constraints from access to the brightest Balmer lines—which correlate best with M_{BH} —at all redshifts; (2) mapping accretion-powered outflows and their physical connection to star-forming regions in the host galaxy to unprecedented precision (Cresci et al. 2023); and (3) constraining host galaxy kinematics with far-IR observations and studying the relation between M_{BH} and the stellar velocity dispersion beyond redshift $z \sim 1$. From both photometric and spectroscopic data, SPS modeling of the host galaxy SEDs would enormously improve in two ways; one in the stronger constraints on star for-

mation histories given by broader wavelength coverage and the incorporation of spectroscopy; and two in the newfound ability to model the SEDs pixel-by-pixel (e.g., Ding et al. 2022) to measure projected distributions of M_{\star} and SFR.

ACKNOWLEDGMENTS

This work was supported by The College Undergraduate program and the Department of Astronomy and Astrophysics at the University of Chicago. APC acknowledges funding from the College Center for Research and Fellowships at the University of Chicago.

We would like to express gratitude towards the staff at the 6.5m Magellan Telescopes at the Las Campanas Observatory, Chile for their valuable labor, and in particular for their care and efforts during a global pandemic.

This paper is partially based on data gathered with the 6.5m Magellan Telescopes located at Las Campanas Observatory, Chile. Magellan observing time for this program was granted by the time allocation committees of the University of Chicago and the University of Michigan.

This paper is partially based on observations made with the Nordic Optical Telescope, owned in collaboration by the University of Turku and Aarhus University, and operated jointly by Aarhus University, the University of Turku and the University of Oslo, representing Denmark, Finland and Norway, the University of Iceland and Stockholm University at the Observatorio del Roque de los Muchachos, La Palma, Spain, of the Instituto de Astrofísica de Canarias. The data presented here were obtained in part with ALFOSC, which is provided by the Instituto de Astrofísica de Andalucía (IAA) under a joint agreement with the University of Copenhagen and NOT.

This paper is partially based on observations made with the NASA/ESA Hubble Space Telescope, obtained from the Multimission Archive at the Space Telescope Science Institute (MAST) at the Space Telescope Science Institute, which is operated by the Association of Universities for Research in Astronomy, Incorporated, under NASA contract NAS 5-26555. These archival observations are associated with programs GO-10509, GO-9744, GO-10793, GO-12195, and GO-13337.

The Legacy Surveys consist of three individual and complementary projects: the Dark Energy Camera Legacy Survey (DECaLS; Proposal ID 2014B-0404; PIs: David Schlegel and Arjun Dey), the Beijing-Arizona Sky Survey (BASS; NOAO Prop. ID 2015A-0801; PIs: Zhou Xu and Xiaohui Fan), and the Mayall z-band Legacy Survey (MzLS; Prop. ID 2016A-0453; PI: Arjun Dey). DECaLS, BASS and MzLS together include data

obtained, respectively, at the Blanco telescope, Cerro Tololo Inter-American Observatory, NSF’s NOIRLab; the Bok telescope, Steward Observatory, University of Arizona; and the Mayall telescope, Kitt Peak National Observatory, NOIRLab. The Legacy Surveys project is honored to be permitted to conduct astronomical research on Iolkam Du’ag (Kitt Peak), a mountain with particular significance to the Tohono O’odham Nation.

NOIRLab is operated by the Association of Universities for Research in Astronomy (AURA) under a cooperative agreement with the National Science Foundation. LBNL is managed by the Regents of the University of California under contract to the U.S. Department of Energy.

This project used data obtained with the Dark Energy Camera (DECam), which was constructed by the Dark Energy Survey (DES) collaboration. Funding for the DES Projects has been provided by the US Department of Energy, the US National Science Foundation, the Ministry of Science and Education of Spain, the Science and Technology Facilities Council of the United Kingdom, the Higher Education Funding Council for England, the National Center for Supercomputing Applications at the University of Illinois at Urbana-Champaign, the Kavli Institute for Cosmological Physics at the University of Chicago, Center for Cosmology and Astro-Particle Physics at the Ohio State University, the Mitchell Institute for Fundamental Physics and Astronomy at Texas A&M University, Financiadora de Estudos e Projetos, Fundação Carlos Chagas Filho de Amparo à Pesquisa do Estado do Rio de Janeiro, Conselho Nacional de Desenvolvimento Científico e Tecnológico and the Ministério da Ciência, Tecnologia e Inovação, the Deutsche Forschungsgemeinschaft and the Collaborating Institutions in the Dark Energy Survey. The Collaborating Institutions are Argonne National Laboratory, the University of California at Santa Cruz, the University of Cambridge, Centro de Investigaciones Enérgéticas, Medioambientales y Tecnológicas–Madrid, the University of Chicago, University College London, the DES-Brazil Consortium, the University of Edinburgh, the Eidgenössische Technische Hochschule (ETH) Zürich, Fermi National Accelerator Laboratory, the University of Illinois at Urbana-Champaign, the Institut de Ciències de l’Espai (IEEC/CSIC), the Institut de Física d’Altes Energies, Lawrence Berkeley National Laboratory, the Ludwig-Maximilians Universität München and the associated Excellence Cluster Universe, the University of Michigan, NSF’s NOIRLab, the University of Nottingham, the Ohio State University, the OzDES Membership Consortium, the University of Pennsylvania, the University of Portsmouth, SLAC National Ac-

celerator Laboratory, Stanford University, the University of Sussex, and Texas A&M University.

BASS is a key project of the Telescope Access Program (TAP), which has been funded by the National Astronomical Observatories of China, the Chinese Academy of Sciences (the Strategic Priority Research Program “The Emergence of Cosmological Structures” Grant # XDB09000000), and the Special Fund for Astronomy from the Ministry of Finance. The BASS is also supported by the External Cooperation Program of Chinese Academy of Sciences (Grant # 114A11KYSB20160057), and Chinese National Natural Science Foundation (Grant # 12120101003, # 11433005).

The Legacy Survey team makes use of data products from the Near-Earth Object Wide-field Infrared Survey Explorer (NEOWISE), which is a project of the Jet Propulsion Laboratory/California Institute of Technology. NEOWISE is funded by the National Aeronautics and Space Administration.

The Legacy Surveys imaging of the DESI footprint is supported by the Director, Office of Science, Office of High Energy Physics of the U.S. Department of Energy under Contract No. DE-AC02- 05CH1123, by the National Energy Research Scientific Computing Center, a DOE Office of Science User Facility under the same contract; and by the U.S. National Science Foundation, Division of Astronomical Sciences under Contract No. AST-0950945 to NOIRLab.

Funding for the Sloan Digital Sky Survey IV has been provided by the Alfred P. Sloan Foundation, the U.S. Department of Energy Office of Science, and the Participating Institutions.

SDSS-IV acknowledges support and resources from the Center for High Performance Computing at the University of Utah. The SDSS website is www.sdss4.org.

SDSS-IV is managed by the Astrophysical Research Consortium for the Participating Institutions of the SDSS Collaboration including the Brazilian Participation Group, the Carnegie Institution for Science, Carnegie Mellon University, Center for Astrophysics | Harvard & Smithsonian, the Chilean Participation Group, the French Participation Group, Instituto de Astrofísica de Canarias, The Johns Hopkins University, Kavli Institute for the Physics and Mathematics of the Universe (IPMU) / University of Tokyo, the Korean Participation Group, Lawrence Berkeley National Laboratory, Leibniz Institut für Astrophysik Potsdam (AIP), Max-Planck-Institut für Astronomie (MPIA Heidelberg), Max-Planck-Institut für Astrophysik (MPA Garching), Max-Planck-Institut für Extraterrestrische Physik (MPE), National Astronomical Observatories of

China, New Mexico State University, New York University, University of Notre Dame, Observatório Nacional / MCTI, The Ohio State University, Pennsylvania State University, Shanghai Astronomical Observatory, United Kingdom Participation Group, Universidad Nacional Autónoma de México, University of Arizona, University of Colorado Boulder, University of Oxford, University of Portsmouth, University of Utah, University of Virginia, University of Washington, University of Wisconsin, Vanderbilt University, and Yale University.

Facilities: Magellan Telescopes 6.5m (Baade/FourStar), Nordic Optical Telescope (ALFOSC, NOTCAM), Keck Observatory (LRIS), *HST*

Software: NumPy (Harris et al. 2020), matplotlib (Hunter 2007), Astropy (Astropy Collaboration et al. 2013, 2018), emcee (Foreman-Mackey et al. 2013) SExtractor (Bertin & Arnouts 1996), GALFIT (Peng et al. 2002, 2010), Prospector (Johnson et al. 2021), dynesty (Speagle 2020), PySpecKit (Ginsburg & Mirocha 2011) SAO Image DS9 (Joye & Mandel 2003), Lenstool (Jullo et al. 2007)

REFERENCES

- Abramson, L. E., Gladders, M. D., Dressler, A., et al. 2016, ApJ, 832, 7, doi: [10.3847/0004-637X/832/1/7](https://doi.org/10.3847/0004-637X/832/1/7)
- Acebron, A., Grillo, C., Bergamini, P., et al. 2022a, ApJ, 926, 86, doi: [10.3847/1538-4357/ac3d35](https://doi.org/10.3847/1538-4357/ac3d35)
- . 2022b, A&A, 668, A142, doi: [10.1051/0004-6361/202244836](https://doi.org/10.1051/0004-6361/202244836)
- Aird, J., Coil, A. L., Moustakas, J., et al. 2012, ApJ, 746, 90, doi: [10.1088/0004-637X/746/1/90](https://doi.org/10.1088/0004-637X/746/1/90)
- Antonucci, R. 1993, ARA&A, 31, 473, doi: [10.1146/annurev.aa.31.090193.002353](https://doi.org/10.1146/annurev.aa.31.090193.002353)
- Astropy Collaboration, Robitaille, T. P., Tollerud, E. J., et al. 2013, A&A, 558, A33, doi: [10.1051/0004-6361/201322068](https://doi.org/10.1051/0004-6361/201322068)
- Astropy Collaboration, Price-Whelan, A. M., Sipőcz, B. M., et al. 2018, AJ, 156, 123, doi: [10.3847/1538-3881/aabc4f](https://doi.org/10.3847/1538-3881/aabc4f)
- Bahcall, J. N., Kirhakos, S., Saxe, D. H., & Schneider, D. P. 1997, ApJ, 479, 642, doi: [10.1086/303926](https://doi.org/10.1086/303926)
- Bayliss, M. B., Sharon, K., Acharyya, A., et al. 2017, ApJL, 845, L14, doi: [10.3847/2041-8213/aa831a](https://doi.org/10.3847/2041-8213/aa831a)
- Bennert, V. N., Auger, M. W., Treu, T., Woo, J.-H., & Malkan, M. A. 2011, ApJ, 742, 107, doi: [10.1088/0004-637X/742/2/107](https://doi.org/10.1088/0004-637X/742/2/107)
- Bennert, V. N., Treu, T., Auger, M. W., et al. 2015, ApJ, 809, 20, doi: [10.1088/0004-637X/809/1/20](https://doi.org/10.1088/0004-637X/809/1/20)
- Bennert, V. N., Treu, T., Ding, X., et al. 2021, ApJ, 921, 36, doi: [10.3847/1538-4357/ac151a](https://doi.org/10.3847/1538-4357/ac151a)
- Bertin, E., & Arnouts, S. 1996, A&AS, 117, 393, doi: [10.1051/aas:1996164](https://doi.org/10.1051/aas:1996164)
- Best, P. N., & Heckman, T. M. 2012, MNRAS, 421, 1569, doi: [10.1111/j.1365-2966.2012.20414.x](https://doi.org/10.1111/j.1365-2966.2012.20414.x)
- Bogdán, Á., Goulding, A. D., Natarajan, P., et al. 2023, Nature Astronomy, doi: [10.1038/s41550-023-02111-9](https://doi.org/10.1038/s41550-023-02111-9)
- Bower, R. G., Benson, A. J., Malbon, R., et al. 2006, MNRAS, 370, 645, doi: [10.1111/j.1365-2966.2006.10519.x](https://doi.org/10.1111/j.1365-2966.2006.10519.x)
- Calzetti, D., Armus, L., Bohlin, R. C., et al. 2000, ApJ, 533, 682, doi: [10.1086/308692](https://doi.org/10.1086/308692)
- Carnall, A. C., Leja, J., Johnson, B. D., et al. 2019, ApJ, 873, 44, doi: [10.3847/1538-4357/ab04a2](https://doi.org/10.3847/1538-4357/ab04a2)
- Chabrier, G. 2003, PASP, 115, 763, doi: [10.1086/376392](https://doi.org/10.1086/376392)
- Coatman, L., Hewett, P. C., Banerji, M., et al. 2017, MNRAS, 465, 2120, doi: [10.1093/mnras/stw2797](https://doi.org/10.1093/mnras/stw2797)
- Conroy, C. 2013, ARA&A, 51, 393, doi: [10.1146/annurev-astro-082812-141017](https://doi.org/10.1146/annurev-astro-082812-141017)
- Cresci, G., Tozzi, G., Perna, M., et al. 2023, A&A, 672, A128, doi: [10.1051/0004-6361/202346001](https://doi.org/10.1051/0004-6361/202346001)
- Croom, S. M., Richards, G. T., Shanks, T., et al. 2009, MNRAS, 399, 1755, doi: [10.1111/j.1365-2966.2009.15398.x](https://doi.org/10.1111/j.1365-2966.2009.15398.x)
- Croton, D. J., Springel, V., White, S. D. M., et al. 2006, MNRAS, 365, 11, doi: [10.1111/j.1365-2966.2005.09675.x](https://doi.org/10.1111/j.1365-2966.2005.09675.x)
- Dahle, H., Gladders, M. D., Sharon, K., Bayliss, M. B., & Rigby, J. R. 2015, ApJ, 813, 67, doi: [10.1088/0004-637X/813/1/67](https://doi.org/10.1088/0004-637X/813/1/67)
- Dahle, H., Gladders, M. D., Sharon, K., et al. 2013, ApJ, 773, 146, doi: [10.1088/0004-637x/773/2/146](https://doi.org/10.1088/0004-637x/773/2/146)
- Dawson, K. S., Kneib, J.-P., Percival, W. J., et al. 2016, AJ, 151, 44, doi: [10.3847/0004-6256/151/2/44](https://doi.org/10.3847/0004-6256/151/2/44)
- Ding, X., Silverman, J. D., & Onoue, M. 2022, ApJL, 939, L28, doi: [10.3847/2041-8213/ac9c02](https://doi.org/10.3847/2041-8213/ac9c02)
- Ding, X., Silverman, J., Treu, T., et al. 2020, ApJ, 888, 37, doi: [10.3847/1538-4357/ab5b90](https://doi.org/10.3847/1538-4357/ab5b90)
- Ding, X., Treu, T., Birrer, S., et al. 2021, MNRAS, 501, 269, doi: [10.1093/mnras/staa2992](https://doi.org/10.1093/mnras/staa2992)
- Dunlop, J. S., McLure, R. J., Kukula, M. J., et al. 2003, MNRAS, 340, 1095, doi: [10.1046/j.1365-8711.2003.06333.x](https://doi.org/10.1046/j.1365-8711.2003.06333.x)
- Fabian, A. C. 2012, ARA&A, 50, 455, doi: [10.1146/annurev-astro-081811-125521](https://doi.org/10.1146/annurev-astro-081811-125521)

- Ferrarese, L., & Merritt, D. 2000, ApJL, 539, L9, doi: [10.1086/312838](https://doi.org/10.1086/312838)
- Fian, C., Muñoz, J. A., Forés-Toribio, R., et al. 2024, A&A, 682, A57, doi: [10.1051/0004-6361/202347382](https://doi.org/10.1051/0004-6361/202347382)
- Fohlmeister, J., Kochanek, C. S., Falco, E. E., et al. 2013, ApJ, 764, 186, doi: [10.1088/0004-637X/764/2/186](https://doi.org/10.1088/0004-637X/764/2/186)
- Foreman-Mackey, D., Hogg, D. W., Lang, D., & Goodman, J. 2013, PASP, 125, 306, doi: [10.1086/670067](https://doi.org/10.1086/670067)
- Furtak, L. J., Labbé, I., Zitrin, A., et al. 2023, arXiv e-prints, arXiv:2308.05735, doi: [10.48550/arXiv.2308.05735](https://doi.org/10.48550/arXiv.2308.05735)
- Ginsburg, A., & Mirocha, J. 2011, PySpecKit: Python Spectroscopic Toolkit, Astrophysics Source Code Library, record ascl:1109.001. <http://ascl.net/1109.001>
- Glikman, E., Simmons, B., Mailly, M., et al. 2015, ApJ, 806, 218, doi: [10.1088/0004-637X/806/2/218](https://doi.org/10.1088/0004-637X/806/2/218)
- Goulding, A. D., Greene, J. E., Setton, D. J., et al. 2023, ApJL, 955, L24, doi: [10.3847/2041-8213/acf7c5](https://doi.org/10.3847/2041-8213/acf7c5)
- Guyon, O., Sanders, D. B., & Stockton, A. 2006, ApJS, 166, 89, doi: [10.1086/505030](https://doi.org/10.1086/505030)
- Habouzit, M., Li, Y., Somerville, R. S., et al. 2021, MNRAS, 503, 1940, doi: [10.1093/mnras/stab496](https://doi.org/10.1093/mnras/stab496)
- Häring, N., & Rix, H.-W. 2004, ApJL, 604, L89, doi: [10.1086/383567](https://doi.org/10.1086/383567)
- Harris, C. R., Millman, K. J., van der Walt, S. J., et al. 2020, Nature, 585, 357, doi: [10.1038/s41586-020-2649-2](https://doi.org/10.1038/s41586-020-2649-2)
- Hartley, P., Jackson, N., Badole, S., et al. 2021, MNRAS, 508, 4625, doi: [10.1093/mnras/stab2758](https://doi.org/10.1093/mnras/stab2758)
- Hopkins, P. F., Hernquist, L., Cox, T. J., et al. 2006, ApJS, 163, 1, doi: [10.1086/499298](https://doi.org/10.1086/499298)
- Hunter, J. D. 2007, Computing in Science Engineering, 9, 90, doi: [10.1109/MCSE.2007.55](https://doi.org/10.1109/MCSE.2007.55)
- Hutsemékers, D., Sluse, D., Savić, Đ., & Richards, G. T. 2023, A&A, 672, A45, doi: [10.1051/0004-6361/202245490](https://doi.org/10.1051/0004-6361/202245490)
- Inada, N., Oguri, M., Pindor, B., et al. 2003, Nature, 426, 810, doi: [10.1038/nature02153](https://doi.org/10.1038/nature02153)
- Inada, N., Oguri, M., Keeton, C. R., et al. 2005, PASJ, 57, L7, doi: [10.1093/pasj/57.3.L7](https://doi.org/10.1093/pasj/57.3.L7)
- Inada, N., Oguri, M., Morokuma, T., et al. 2006, ApJL, 653, L97, doi: [10.1086/510671](https://doi.org/10.1086/510671)
- Johnson, B. D., Leja, J., Conroy, C., & Speagle, J. S. 2021, ApJS, 254, 22, doi: [10.3847/1538-4365/abef67](https://doi.org/10.3847/1538-4365/abef67)
- Joye, W. A., & Mandel, E. 2003, in Astronomical Society of the Pacific Conference Series, Vol. 295, Astronomical Data Analysis Software and Systems XII, ed. H. E. Payne, R. I. Jedrzejewski, & R. N. Hook, 489
- Jullo, E., Kneib, J. P., Limousin, M., et al. 2007, New Journal of Physics, 9, 447, doi: [10.1088/1367-2630/9/12/447](https://doi.org/10.1088/1367-2630/9/12/447)
- Kakkad, D., Mainieri, V., Vietri, G., et al. 2023, MNRAS, 520, 5783, doi: [10.1093/mnras/stad439](https://doi.org/10.1093/mnras/stad439)
- Kelly, B. C., & Shen, Y. 2013, ApJ, 764, 45, doi: [10.1088/0004-637X/764/1/45](https://doi.org/10.1088/0004-637X/764/1/45)
- Khullar, G., Gozman, K., Lin, J. J., et al. 2021, ApJ, 906, 107, doi: [10.3847/1538-4357/abcb86](https://doi.org/10.3847/1538-4357/abcb86)
- King, A., & Pounds, K. 2015, ARA&A, 53, 115, doi: [10.1146/annurev-astro-082214-122316](https://doi.org/10.1146/annurev-astro-082214-122316)
- Kirkpatrick, A., Urry, C. M., Brewster, J., et al. 2020, ApJ, 900, 5, doi: [10.3847/1538-4357/aba358](https://doi.org/10.3847/1538-4357/aba358)
- Kisare, A., Gladders, M. D., Napier, K. A., et al. in prep., for submission to AAS Journals
- Klein, M., Sharon, K., Napier, K., et al. 2024, arXiv e-prints, arXiv:2401.10168, doi: [10.48550/arXiv.2401.10168](https://doi.org/10.48550/arXiv.2401.10168)
- Kocevski, D. D., Barro, G., McGrath, E. J., et al. 2023, ApJL, 946, L14, doi: [10.3847/2041-8213/acad00](https://doi.org/10.3847/2041-8213/acad00)
- Kormendy, J., & Ho, L. C. 2013, ARA&A, 51, 511, doi: [10.1146/annurev-astro-082708-101811](https://doi.org/10.1146/annurev-astro-082708-101811)
- Koss, M. J., Ricci, C., Trakhtenbrot, B., et al. 2022, ApJS, 261, 2, doi: [10.3847/1538-4365/ac6c05](https://doi.org/10.3847/1538-4365/ac6c05)
- Kriek, M., & Conroy, C. 2013, ApJL, 775, L16, doi: [10.1088/2041-8205/775/1/L16](https://doi.org/10.1088/2041-8205/775/1/L16)
- Larson, R. L., Finkelstein, S. L., Kocevski, D. D., et al. 2023, ApJL, 953, L29, doi: [10.3847/2041-8213/ace619](https://doi.org/10.3847/2041-8213/ace619)
- Lauer, T. R., Tremaine, S., Richstone, D., & Faber, S. M. 2007, ApJ, 670, 249, doi: [10.1086/522083](https://doi.org/10.1086/522083)
- Leja, J., Speagle, J. S., Ting, Y.-S., et al. 2022, ApJ, 936, 165, doi: [10.3847/1538-4357/ac887d](https://doi.org/10.3847/1538-4357/ac887d)
- Lemon, C., Anguita, T., Auger-Williams, M. W., et al. 2023, MNRAS, 520, 3305, doi: [10.1093/mnras/stac3721](https://doi.org/10.1093/mnras/stac3721)
- Li, J., Silverman, J. D., Shen, Y., et al. 2024, arXiv e-prints, arXiv:2403.00074, doi: [10.48550/arXiv.2403.00074](https://doi.org/10.48550/arXiv.2403.00074)
- Li, J. I. H., Shen, Y., Ho, L. C., et al. 2023, ApJ, 954, 173, doi: [10.3847/1538-4357/acddd4](https://doi.org/10.3847/1538-4357/acddd4)
- Lower, S., Narayanan, D., Leja, J., et al. 2020, ApJ, 904, 33, doi: [10.3847/1538-4357/abbfa7](https://doi.org/10.3847/1538-4357/abbfa7)
- Lusso, E., Comastri, A., Simmons, B. D., et al. 2012, MNRAS, 425, 623, doi: [10.1111/j.1365-2966.2012.21513.x](https://doi.org/10.1111/j.1365-2966.2012.21513.x)
- Lynden-Bell, D. 1969, Nature, 223, 690, doi: [10.1038/223690a0](https://doi.org/10.1038/223690a0)
- Magorrian, J., Tremaine, S., Richstone, D., et al. 1998, AJ, 115, 2285, doi: [10.1086/300353](https://doi.org/10.1086/300353)
- Maiolino, R., Scholtz, J., Curtis-Lake, E., et al. 2023, arXiv e-prints, arXiv:2308.01230, doi: [10.48550/arXiv.2308.01230](https://doi.org/10.48550/arXiv.2308.01230)
- Marconi, A., & Hunt, L. K. 2003, ApJL, 589, L21, doi: [10.1086/375804](https://doi.org/10.1086/375804)
- Marconi, A., Risaliti, G., Gilli, R., et al. 2004, MNRAS, 351, 169, doi: [10.1111/j.1365-2966.2004.07765.x](https://doi.org/10.1111/j.1365-2966.2004.07765.x)

- Marshall, M. A., Perna, M., Willott, C. J., et al. 2023, *A&A*, 678, A191, doi: [10.1051/0004-6361/202346113](https://doi.org/10.1051/0004-6361/202346113)
- Martinez, M. N., Napier, K. A., Cloonan, A. P., et al. 2023, *ApJ*, 946, 63, doi: [10.3847/1538-4357/acbe39](https://doi.org/10.3847/1538-4357/acbe39)
- McKean, J. P., Luichies, R., Drabent, A., et al. 2021, *MNRAS*, 505, L36, doi: [10.1093/mnrasl/slab033](https://doi.org/10.1093/mnrasl/slab033)
- McKinney, J., Hayward, C. C., Rosenthal, L. J., et al. 2021, *ApJ*, 921, 55, doi: [10.3847/1538-4357/ac185f](https://doi.org/10.3847/1538-4357/ac185f)
- Mejía-Restrepo, J. E., Trakhtenbrot, B., Lira, P., Netzer, H., & Capellupo, D. M. 2016, *MNRAS*, 460, 187, doi: [10.1093/mnras/stw568](https://doi.org/10.1093/mnras/stw568)
- Merloni, A., Bongiorno, A., Bolzonella, M., et al. 2010, *ApJ*, 708, 137, doi: [10.1088/0004-637X/708/1/137](https://doi.org/10.1088/0004-637X/708/1/137)
- Moffat, A. F. J. 1969, *A&A*, 3, 455
- Muñoz, J. A., Kochanek, C. S., Fohlmeister, J., et al. 2022, *ApJ*, 937, 34, doi: [10.3847/1538-4357/ac8877](https://doi.org/10.3847/1538-4357/ac8877)
- Mullaney, J. R., Daddi, E., Béthermin, M., et al. 2012, *ApJL*, 753, L30, doi: [10.1088/2041-8205/753/2/L30](https://doi.org/10.1088/2041-8205/753/2/L30)
- Napier, K., Sharon, K., Dahle, H., et al. 2023a, *ApJ*, 959, 134, doi: [10.3847/1538-4357/ad045a](https://doi.org/10.3847/1538-4357/ad045a)
- Napier, K., Gladders, M. D., Sharon, K., et al. 2023b, *ApJL*, 954, L38, doi: [10.3847/2041-8213/acf132](https://doi.org/10.3847/2041-8213/acf132)
- Netzer, H. 2015, *ARA&A*, 53, 365, doi: [10.1146/annurev-astro-082214-122302](https://doi.org/10.1146/annurev-astro-082214-122302)
- Ogawa, S., Ueda, Y., Tanimoto, A., & Yamada, S. 2021, *ApJ*, 906, 84, doi: [10.3847/1538-4357/abccce](https://doi.org/10.3847/1538-4357/abccce)
- Oguri, M., Schrabback, T., Jullo, E., et al. 2013, *MNRAS*, 429, 482, doi: [10.1093/mnras/sts351](https://doi.org/10.1093/mnras/sts351)
- Oke, J. B., Cohen, J. G., Carr, M., et al. 1995, *PASP*, 107, 375, doi: [10.1086/133562](https://doi.org/10.1086/133562)
- Omont, A., Petitjean, P., Guilloteau, S., et al. 1996, *Nature*, 382, 428, doi: [10.1038/382428a0](https://doi.org/10.1038/382428a0)
- Pacucci, F., Nguyen, B., Carmiani, S., Maiolino, R., & Fan, X. 2023, *ApJL*, 957, L3, doi: [10.3847/2041-8213/ad0158](https://doi.org/10.3847/2041-8213/ad0158)
- Padovani, P., Alexander, D. M., Assef, R. J., et al. 2017, *A&A Rv*, 25, 2, doi: [10.1007/s00159-017-0102-9](https://doi.org/10.1007/s00159-017-0102-9)
- Peng, C. Y., Ho, L. C., Impey, C. D., & Rix, H.-W. 2002, *AJ*, 124, 266, doi: [10.1086/340952](https://doi.org/10.1086/340952)
- . 2010, *AJ*, 139, 2097, doi: [10.1088/0004-6256/139/6/2097](https://doi.org/10.1088/0004-6256/139/6/2097)
- Peng, C. Y., Impey, C. D., Rix, H.-W., et al. 2006, *ApJ*, 649, 616, doi: [10.1086/506266](https://doi.org/10.1086/506266)
- Peterson, B. M. 1993, *PASP*, 105, 247, doi: [10.1086/133140](https://doi.org/10.1086/133140)
- Popesso, P., Concas, A., Cresci, G., et al. 2023, *MNRAS*, 519, 1526, doi: [10.1093/mnras/stac3214](https://doi.org/10.1093/mnras/stac3214)
- Ricci, C., Ueda, Y., Koss, M. J., et al. 2015, *ApJL*, 815, L13, doi: [10.1088/2041-8205/815/1/L13](https://doi.org/10.1088/2041-8205/815/1/L13)
- Richards, G. T., Lacy, M., Storrie-Lombardi, L. J., et al. 2006, *ApJS*, 166, 470, doi: [10.1086/506525](https://doi.org/10.1086/506525)
- Ross, N. R., Assef, R. J., Kochanek, C. S., Falco, E., & Poindexter, S. D. 2009, *ApJ*, 702, 472, doi: [10.1088/0004-637X/702/1/472](https://doi.org/10.1088/0004-637X/702/1/472)
- Sajina, A., Lacy, M., & Pope, A. 2022, *Universe*, 8, 356, doi: [10.3390/universe8070356](https://doi.org/10.3390/universe8070356)
- Santini, P., Ferguson, H. C., Fontana, A., et al. 2015, *ApJ*, 801, 97, doi: [10.1088/0004-637X/801/2/97](https://doi.org/10.1088/0004-637X/801/2/97)
- Schneider, R., Valiante, R., Trinca, A., et al. 2023, *MNRAS*, 526, 3250, doi: [10.1093/mnras/stad2503](https://doi.org/10.1093/mnras/stad2503)
- Schramm, M., & Silverman, J. D. 2013, *ApJ*, 767, 13, doi: [10.1088/0004-637X/767/1/13](https://doi.org/10.1088/0004-637X/767/1/13)
- Schulze, A., & Wisotzki, L. 2011, *A&A*, 535, A87, doi: [10.1051/0004-6361/201117564](https://doi.org/10.1051/0004-6361/201117564)
- . 2014, *MNRAS*, 438, 3422, doi: [10.1093/mnras/stt2457](https://doi.org/10.1093/mnras/stt2457)
- Schulze, A., Bongiorno, A., Gavignaud, I., et al. 2015, *MNRAS*, 447, 2085, doi: [10.1093/mnras/stu2549](https://doi.org/10.1093/mnras/stu2549)
- Shankar, F., Weinberg, D. H., Marsden, C., et al. 2020, *MNRAS*, 493, 1500, doi: [10.1093/mnras/stz3522](https://doi.org/10.1093/mnras/stz3522)
- Sharon, K., Bayliss, M. B., Dahle, H., et al. 2017, *ApJ*, 835, 5, doi: [10.3847/1538-4357/835/1/5](https://doi.org/10.3847/1538-4357/835/1/5)
- Shen, Y. 2016, *ApJ*, 817, 55, doi: [10.3847/0004-637X/817/1/55](https://doi.org/10.3847/0004-637X/817/1/55)
- Shen, Y., Richards, G. T., Strauss, M. A., et al. 2011, *ApJS*, 194, 45, doi: [10.1088/0067-0049/194/2/45](https://doi.org/10.1088/0067-0049/194/2/45)
- Shu, Y., Koposov, S. E., Evans, N. W., et al. 2019, *MNRAS*, 489, 4741, doi: [10.1093/mnras/stz2487](https://doi.org/10.1093/mnras/stz2487)
- Shu, Y., Marques-Chaves, R., Evans, N. W., & Pérez-Fournon, I. 2018, *MNRAS*, 481, L136, doi: [10.1093/mnras/sly174](https://doi.org/10.1093/mnras/sly174)
- Simmons, B. D., Urry, C. M., Schawinski, K., Cardamone, C., & Glikman, E. 2012, *ApJ*, 761, 75, doi: [10.1088/0004-637X/761/1/75](https://doi.org/10.1088/0004-637X/761/1/75)
- Skrutskie, M. F., Cutri, R. M., Stiening, R., et al. 2006, *AJ*, 131, 1163, doi: [10.1086/498708](https://doi.org/10.1086/498708)
- Smee, S. A., Gunn, J. E., Uomoto, A., et al. 2013, *AJ*, 146, 32, doi: [10.1088/0004-6256/146/2/32](https://doi.org/10.1088/0004-6256/146/2/32)
- Somerville, R. S., Hopkins, P. F., Cox, T. J., Robertson, B. E., & Hernquist, L. 2008, *MNRAS*, 391, 481, doi: [10.1111/j.1365-2966.2008.13805.x](https://doi.org/10.1111/j.1365-2966.2008.13805.x)
- Speagle, J. S. 2020, *MNRAS*, 493, 3132, doi: [10.1093/mnras/staa278](https://doi.org/10.1093/mnras/staa278)
- Speagle, J. S., Steinhardt, C. L., Capak, P. L., & Silverman, J. D. 2014, *ApJS*, 214, 15, doi: [10.1088/0067-0049/214/2/15](https://doi.org/10.1088/0067-0049/214/2/15)
- Stacey, H. R., McKean, J. P., Robertson, N. C., et al. 2018, *MNRAS*, 476, 5075, doi: [10.1093/mnras/sty458](https://doi.org/10.1093/mnras/sty458)
- Stacey, H. R., McKean, J. P., Powell, D. M., et al. 2020, *MNRAS*, 500, 3667, doi: [10.1093/mnras/staa3433](https://doi.org/10.1093/mnras/staa3433)

- Stone, M. A., Lyu, J., Rieke, G. H., Alberts, S., & Hainline, K. N. 2023, arXiv e-prints, arXiv:2310.18395, doi: [10.48550/arXiv.2310.18395](https://doi.org/10.48550/arXiv.2310.18395)
- Suh, H., Civano, F., Trakhtenbrot, B., et al. 2020, ApJ, 889, 32, doi: [10.3847/1538-4357/ab5f5f](https://doi.org/10.3847/1538-4357/ab5f5f)
- Takahashi, R., Oguri, M., Sato, M., & Hamana, T. 2011, ApJ, 742, 15, doi: [10.1088/0004-637X/742/1/15](https://doi.org/10.1088/0004-637X/742/1/15)
- Tanaka, T. S., Silverman, J. D., Ding, X., et al. 2024, arXiv e-prints, arXiv:2401.13742, doi: [10.48550/arXiv.2401.13742](https://doi.org/10.48550/arXiv.2401.13742)
- Tarrío, P., Melin, J. B., & Arnaud, M. 2019, A&A, 626, A7, doi: [10.1051/0004-6361/201834979](https://doi.org/10.1051/0004-6361/201834979)
- Tody, D. 1986, in Society of Photo-Optical Instrumentation Engineers (SPIE) Conference Series, Vol. 627, Instrumentation in astronomy VI, ed. D. L. Crawford, 733, doi: [10.1117/12.968154](https://doi.org/10.1117/12.968154)
- Trakhtenbrot, B., & Netzer, H. 2012, MNRAS, 427, 3081, doi: [10.1111/j.1365-2966.2012.22056.x](https://doi.org/10.1111/j.1365-2966.2012.22056.x)
- Veilleux, S., Maiolino, R., Bolatto, A. D., & Aalto, S. 2020, A&A Rv, 28, 2, doi: [10.1007/s00159-019-0121-9](https://doi.org/10.1007/s00159-019-0121-9)
- Venemans, B. P., Walter, F., Decarli, R., et al. 2017, ApJ, 845, 154, doi: [10.3847/1538-4357/aa81cb](https://doi.org/10.3847/1538-4357/aa81cb)
- Vestergaard, M. 2002, ApJ, 571, 733, doi: [10.1086/340045](https://doi.org/10.1086/340045)
- Wagg, J., Wiklind, T., Carilli, C. L., et al. 2012, ApJL, 752, L30, doi: [10.1088/2041-8205/752/2/L30](https://doi.org/10.1088/2041-8205/752/2/L30)
- Wandel, A., Peterson, B. M., & Malkan, M. A. 1999, ApJ, 526, 579, doi: [10.1086/308017](https://doi.org/10.1086/308017)
- Wang, F., Yang, J., Hennawi, J. F., et al. 2023, ApJL, 951, L4, doi: [10.3847/2041-8213/accd6f](https://doi.org/10.3847/2041-8213/accd6f)
- Weaver, J. R., Davidzon, I., Toft, S., et al. 2023, A&A, 677, A184, doi: [10.1051/0004-6361/202245581](https://doi.org/10.1051/0004-6361/202245581)
- Wellons, S., Faucher-Giguère, C.-A., Hopkins, P. F., et al. 2023, MNRAS, 520, 5394, doi: [10.1093/mnras/stad511](https://doi.org/10.1093/mnras/stad511)
- Whitaker, K. E., Franx, M., Leja, J., et al. 2014, ApJ, 795, 104, doi: [10.1088/0004-637X/795/2/104](https://doi.org/10.1088/0004-637X/795/2/104)
- Williams, P. R., Treu, T., Dahle, H., et al. 2021a, ApJ, 911, 64, doi: [10.3847/1538-4357/abe943](https://doi.org/10.3847/1538-4357/abe943)
- . 2021b, ApJL, 915, L9, doi: [10.3847/2041-8213/ac081b](https://doi.org/10.3847/2041-8213/ac081b)
- Yang, G., Brandt, W. N., Vito, F., et al. 2018, MNRAS, 475, 1887, doi: [10.1093/mnras/stx2805](https://doi.org/10.1093/mnras/stx2805)
- Young, J. E., Eracleous, M., Shemmer, O., et al. 2014, MNRAS, 438, 217, doi: [10.1093/mnras/stt2145](https://doi.org/10.1093/mnras/stt2145)
- Zhuang, M.-Y., & Shen, Y. 2023, arXiv e-prints, arXiv:2304.13776, doi: [10.48550/arXiv.2304.13776](https://doi.org/10.48550/arXiv.2304.13776)

APPENDIX

A. FORWARD-MODELING OF SELECTION EFFECTS

Here we outline how we estimate selection bias (Lauer et al. 2007), the method for which is based on that of Schulze & Wisotzki (2011, 2014) (in particular, the ‘flux-limited’ variant introduced in their Section 3). Their formalism allows for computation of an observed bivariate distribution function in M_\star and M_{BH} , given: a local $M_{\text{BH}}-M_\star$ relation, a galaxy stellar mass function (GSMF), an AGN duty cycle (the fraction of SMBHs that are actively accreting) as a function of M_{BH} , an Eddington ratio distribution function (ERDF), and a observational selection function. In our adaptation of this framework, for a given AGN sample we adopt a characteristic redshift (approximately the median) and forward-model a population of broad-line AGNs. For the mock dataset, we compute an average offset $\Delta \log(M_{\text{BH}}/M_\star)$, which corresponds to the offset we would expect to measure assuming no intrinsic evolution in the $M_{\text{BH}}-M_\star$ relation. The advantage of this technique is that it assumes little about available observational data. Even though we obviously do not have data for a large population of magnified quasars, this method can uncover information about the intrinsic selection effects in the WSLQ sample regardless. The input redshifts, selection functions, and predicted offsets for each AGN sample are listed in Table A1. Note that these predicted offsets are what we use in our recalculation of cosmic evolution in the $M_{\text{BH}}-M_\star$ relation from Section 4.2.

We use the following cosmological assumptions: (1) our measurement of the local relation as in Equation (5), with $\alpha_1 = 7.02 \pm 0.38$, $\beta_1 = 0.97 \pm 0.11$ and intrinsic scatter $\sigma_{\text{int}} = 0.37 \pm 0.05$; (2) the GSMF from Weaver et al. (2023), who fit a double Schechter function to each redshift bin; (3) the ERDF from Kelly & Shen (2013), for which we fit a broken power-law model to each redshift bin; and (4) a constant AGN duty cycle of $p_{\text{ac}} = 0.1$. The GSMF is shown in the upper panel of Figure A1, while the ERDF is shown (albeit rescaled) in Figure A2. The lattermost assumption of a constant duty cycle is a simplification that is fairly consistent with observational data of optically luminous broad-line quasars at $z \sim 2$ (e.g., Kelly & Shen 2013). We qualify that this approximation may begin to break down prior to $z = 2$, where the most massive SMBHs appear more likely to be AGNs than less massive ones (Schulze et al. 2015).

We carry out the forward modeling as follows. A random array of mock galaxies with stellar masses M_\star is drawn from the GSMF at the appropriate redshift. Black hole masses M_{BH} are computed via the local $M_{\text{BH}}-M_\star$ relation:

$$\log\left(\frac{M_{\text{BH}}}{M_\odot}\right) = 7.02 + 0.97 \log\left(\frac{M_\star}{10^{10} M_\odot}\right) + n(\sigma_{\text{int}}) + n(\sigma_{\text{se}}), \quad (\text{A1})$$

where we add two random Gaussian numbers: one representing our estimate for the intrinsic scatter $\sigma_{\text{int}} = 0.37$ in $M_{\text{BH}}-M_\star$, and the other representing the scatter $\sigma_{\text{se}} = 0.33$ in the single-epoch M_{BH} measurements (Trakhtenbrot & Netzer 2012). Then, as we have assumed $p_{\text{ac}} = 0.1$, a random 10% of the galaxies are assumed to host broad-line quasars. For these mock quasars, we randomly generate Eddington ratios in the range $\log \lambda_{\text{Edd}} \in [-2, 1]$, weighted by the ERDF. At this point, bolometric luminosities are given as in Schulze & Wisotzki (2011) by:

$$\log L_{\text{bol}} = \log \lambda_{\text{Edd}} + \log M_{\text{BH}} + 38.1. \quad (\text{A2})$$

Finally, we select the mock population according to the selection function shown in Table A1. Regarding this step, we note that the WSLQ selection function is more complex than those of the examples from Schulze & Wisotzki (2011) because we select WSLQs using image-plane, magnified quasar photometry (Martinez et al. 2023; Napier et al. 2023b; Kisare et al. in prep.). Therefore, the WSLQ selection function is dependent on both observed flux and on lensing magnification, as opposed to simply on observed flux as in Merloni et al. (2010) or on intrinsic parameters (M_{BH} , Eddington ratio, AGN X-ray or bolometric luminosity) as in the papers for the other samples we employ (Bennert et al. 2011; Schramm & Silverman 2013, D20).

As an input for lensing magnification for the WSLQ sample, we apply a smoothing kernel to a $z = 2$ magnification distribution function, computed numerically by Takahashi et al. (2011) via ray-tracing simulations, such as to avoid overfitting and better approximate a ‘shape’ of the distribution.¹ This smoothed distribution function is visualized in the top panel of Figure A2. For

¹ We remove the contribution from what Takahashi et al. (2011) refer to as ‘Type I’ lensing. In their terminology, ‘Types II and III’ correspond to what is frequently called strong lensing. We direct readers toward their paper for further details.

AGN Sample	Redshift	Selection Function	Predicted Offset
Schramm & Silverman (2013)	0.8	($43.7 < \log L_{\text{bol}} < 45.7$) and ($7.0 < \log M_{\text{BH}} < 9.4$)	+0.18
Bennert et al. (2011)	1.2	($43.5 < \log L_X < 44.5$) and ($\log M_{\text{BH}} > 7.8$)	+0.38
Ding et al. (2020)	1.5	($7.7 < \log M_{\text{BH}} < 8.8$) and ($45 < \log L_{\text{bol}} < 46.2$) and ($-2 < \log \lambda_{\text{Edd}} < 0.5$)	+0.39
WSLQs (this work)	2.1	($3 < \mu_m < 30.5$) and ($18.4 < r_{\text{img}} < 22.12$)	+0.43

Table A1. Inputs and output offset for modeling selection bias of each sample at redshift $z > 0.5$, given the GSMF and ERDF each as a function of redshift. From left to right, the columns are: the paper of the given AGN sample, the characteristic (median) redshift of the AGN sample, the selection function for each sample as outlined in the corresponding paper, and the expected offset assuming no cosmic evolution in the $M_{\text{BH}}-M_*$ relation. Note that for the literature samples (Schramm & Silverman 2013; Bennert et al. 2011, D20), we shift the M_{BH} cuts slightly to reflect the recalibration to the framework from Trakhtenbrot & Netzer (2012) (see our Section 3.3.2). For the Bennert et al. (2011) sample, L_X is the X-ray luminosity over the 0.5 – 8 keV range, and we calculate this luminosity using a bolometric correction from Lusso et al. (2012).

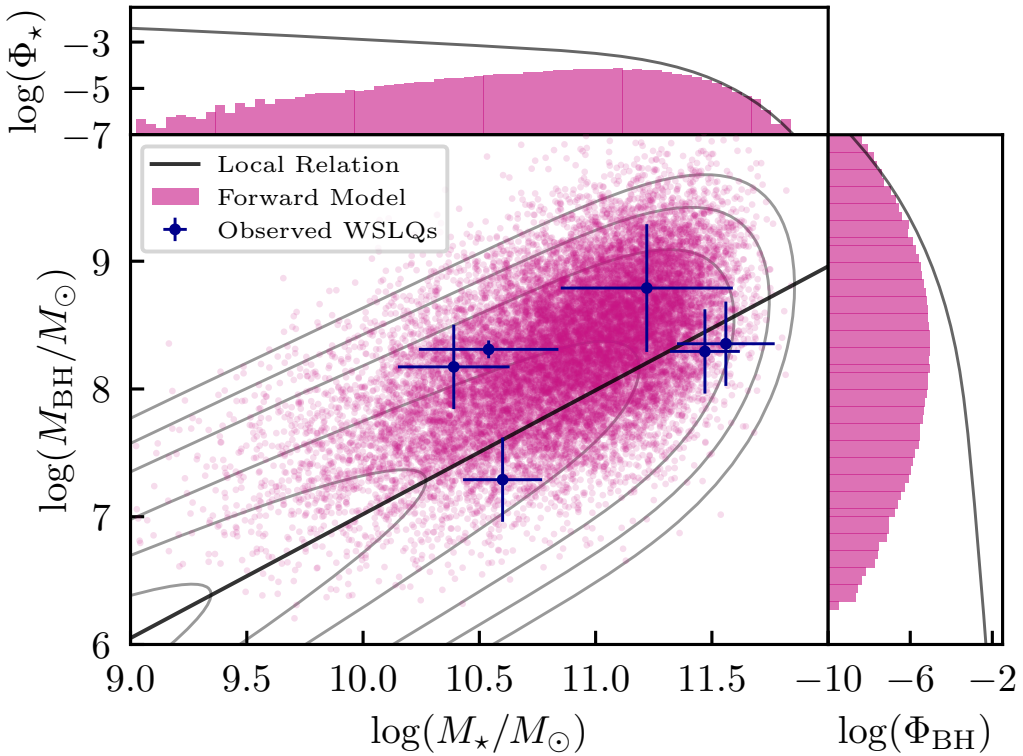


Figure A1. Forward modeling of a population of highly magnified quasars, akin to WSLQs, in $M_{\text{BH}}-M_*$ parameter space. **(Center)** The magenta scatter plot are the mock quasars, while the navy datapoints are the observed WSLQs studied in this paper. The black log-linear line is the measured local relation with slope 0.97 and intercept 7.02, used as an input in the forward modeling framework. The grey contours represent the bivariate distribution function in $M_{\text{BH}}-M_*$ parameter space, which we compute while accounting for the single-epoch M_{BH} uncertainty—see Section 3.4 and Eq. 24 in Schulze & Wisotzki (2011). **(Top)** The projection of bivariate distributions to the galaxy stellar mass, i.e., the GSMF in grey (solid line) and the ‘observed’ M_* distribution of mock quasar host galaxies in magenta. The mock observed distribution is rescaled to emphasize the similarities and differences in shape with the GSMF. **(Right)** The projection in black hole mass, i.e., the black hole mass function in grey (solid line) and the ‘observed’ M_{BH} distribution of mock quasars in magenta (again rescaled).

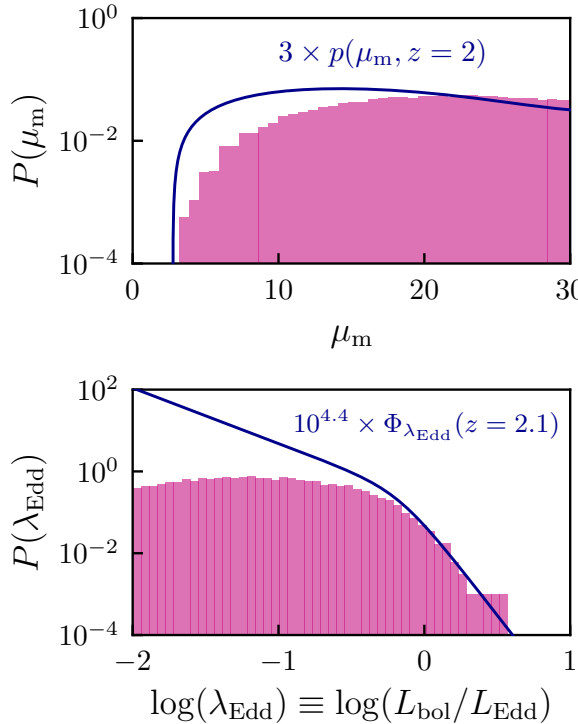


Figure A2. The input distributions for lensing magnification μ_m (**top**) and Eddington ratio λ_{Edd} (**bottom**) used in the forward modeling framework, plotted against the respective histograms for the mock sample of magnified quasars. Each of the input distributions are rescaled for the sake of comparing the shapes of intrinsic vs. ‘observed’ distributions, as in Figure A1. Note that $p(\mu_m)$ is a *probability* distribution while $\Phi_{\lambda_{\text{Edd}}}$ is a physical distribution function like the GSMF.

the image-plane flux, we convert L_{bol} to r -band magnitudes using a K -correction from Croom et al. (2009) of $K(z) = -2.5(1 + \alpha_\nu) \log(1 + z)$ (where α_ν is the spectral index) and the composite optically luminous quasar SED from Richards et al. (2006), which has a spectral index of $\alpha_\nu = -0.5 \pm 0.3$. Like in Equation (A1), we include the ± 0.3 uncertainty by adding random Gaussian numbers $n(\sigma_{\alpha_\nu} = 0.3)$ to mock spectral indices used in the conversion. Then, we magnify these r -band magnitudes with randomly drawn magnification values weighted by the smoothed distribution function from Takahashi et al. (2011). The simulated population of magnified quasars are those systems with $18.40 < r_{\text{img}} < 22.12$ and $3 < \mu_m < 30.5$, which are plotted in Figure A1. This selection function corresponds to the image-plane r -band magnitudes and magnifications of the brightest WSLQ images.

From this forward-modeling analysis, we obtain an expected bias of $+0.43$ in $\Delta \log(M_{\text{BH}}/M_\star)$ for a mock sample of highly magnified quasars at $z \sim 2.1$. For WSLQs

and other samples of highly magnified quasars, then, an observed average $\Delta \log(M_{\text{BH}}/M_\star)$ of $+0.43$ could be interpreted as consistent with a constant $M_{\text{BH}}-M_\star$ relation from $z = 2.1$ to $z = 0$. The model population of magnified quasars is shown in Figure A1, with observed WSLQs plotted over it. There may be a small difference in the $M_{\text{BH}}-M_\star$ parameter space between the model and the observed WSLQs, although we note that they are still consistent; each observed WSLQ is located well within 2σ of the model in $\Delta \log(M_{\text{BH}}/M_\star)$.

We again qualify that our model for selection bias contains uncertainty yet unaccounted for. We hypothesize that the most prominent sources of uncertainty in these computations are (1) the selection functions themselves, which may be incomplete as presented and utilized here; (2) the possible X-ray–radio dichotomy with regards to AGN selection (e.g., Aird et al. 2012; Best & Heckman 2012); (3) the intrinsic scatter in M_{BH} from single-epoch spectroscopy; and for the WSLQ sample (4) the propagation of r -band magnitudes given L_{bol} , as the quasar K -corrections contain some uncertainty. (The formula we apply here was originally used for i -band magnitudes.) Although the duty cycle is dependent on M_{BH} (Schulze et al. 2015), including this dependence does not significantly impact the measured bias; uncertainties in the GSMF and ERDF that we employ also do not.

B. GALLERY OF QUASAR SPECTRA AND GALAXY SEDS

We present all quasar spectra used for M_{BH} measurements in Figure B1 and all host galaxy SEDs modeled with `Prospector` in Figure B2.

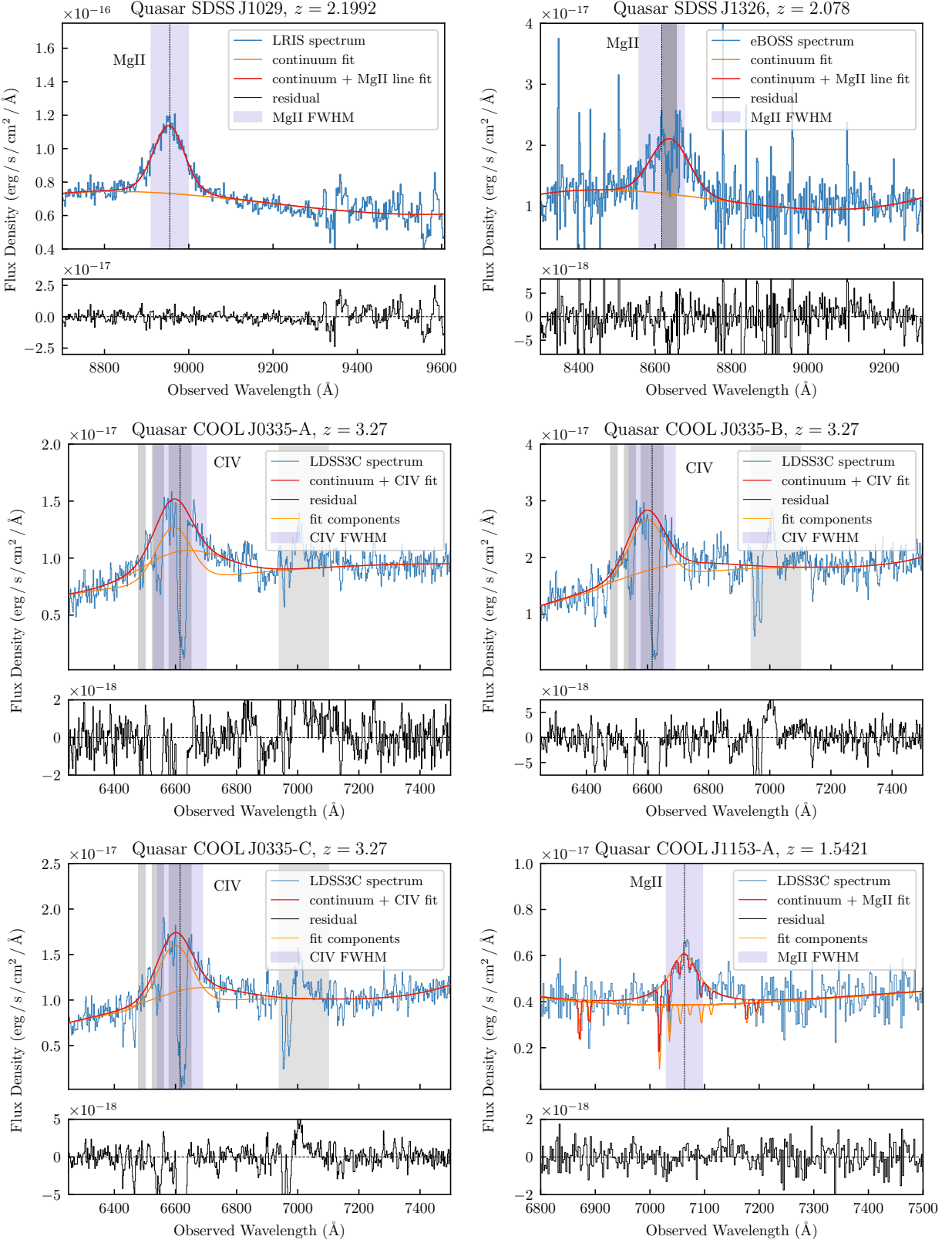


Figure B1. A gallery of quasar spectra and our best-fit models to observed broad emission lines, from which we derive SMBH masses. Note that we model emission for three distinct quasar images of CJ0335, and for SDSS J1029+2623 images of SJ1004, for the purposes of testing systematics in Section 5.1.1. Different images are labeled as A, B, and C, and they are defined visually in Figure 1. For all quasars except for CJ0335 (where we use CIV), we fit the broad MgII emission line. Regions highlighted in grey are those which are masked when fitting. We mask some spectral features for SJ1326 and CJ0335 because the underlying emission line can be easily separated, but we fit intervening candidate absorption simultaneously for CJ1153 given the equal spacing and flux-blending with the MgII emission.

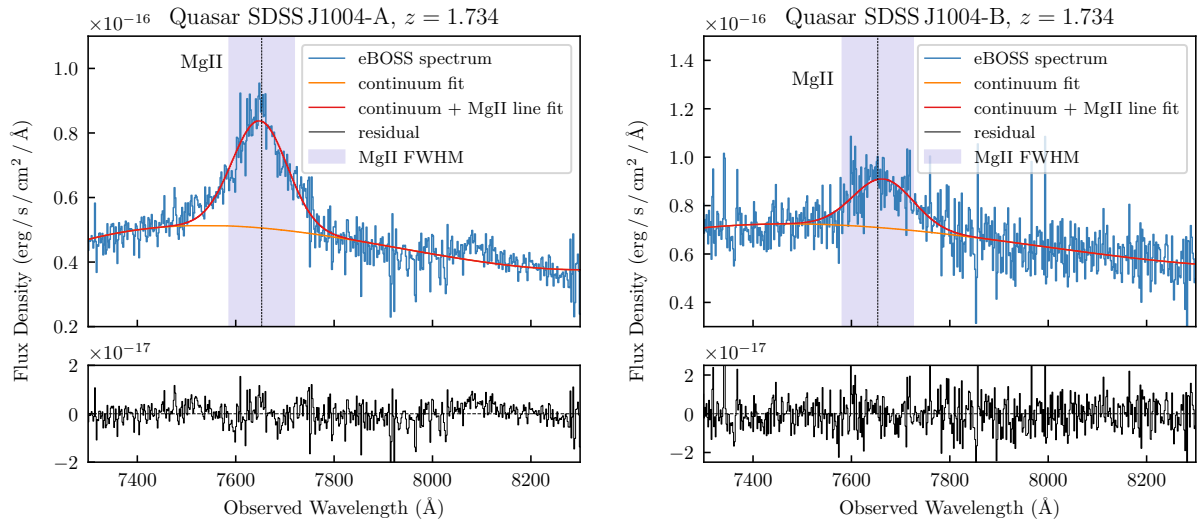


Figure B1. (continued) A gallery of quasar spectra and our best-fit models to observed broad emission lines, from which we derive SMBH masses. Note that we model emission for three distinct quasar images of CJ0335, and for SDSS J1029+2623 images of SJ1004, for the purposes of testing systematics in Section 5.1.1. Different images are labeled as A, B, and C, and they are defined visually in Figure 1. For all quasars except for CJ0335 (where we use CIV), we fit the broad MgII emission line. Regions highlighted in grey are those which are masked during the fitting. We mask some spectral features for SJ1326 and CJ0335 because the underlying emission line can be easily separated, but we fit intervening candidate absorption simultaneously for CJ1153 given the equal spacing and flux-blending with the MgII emission.

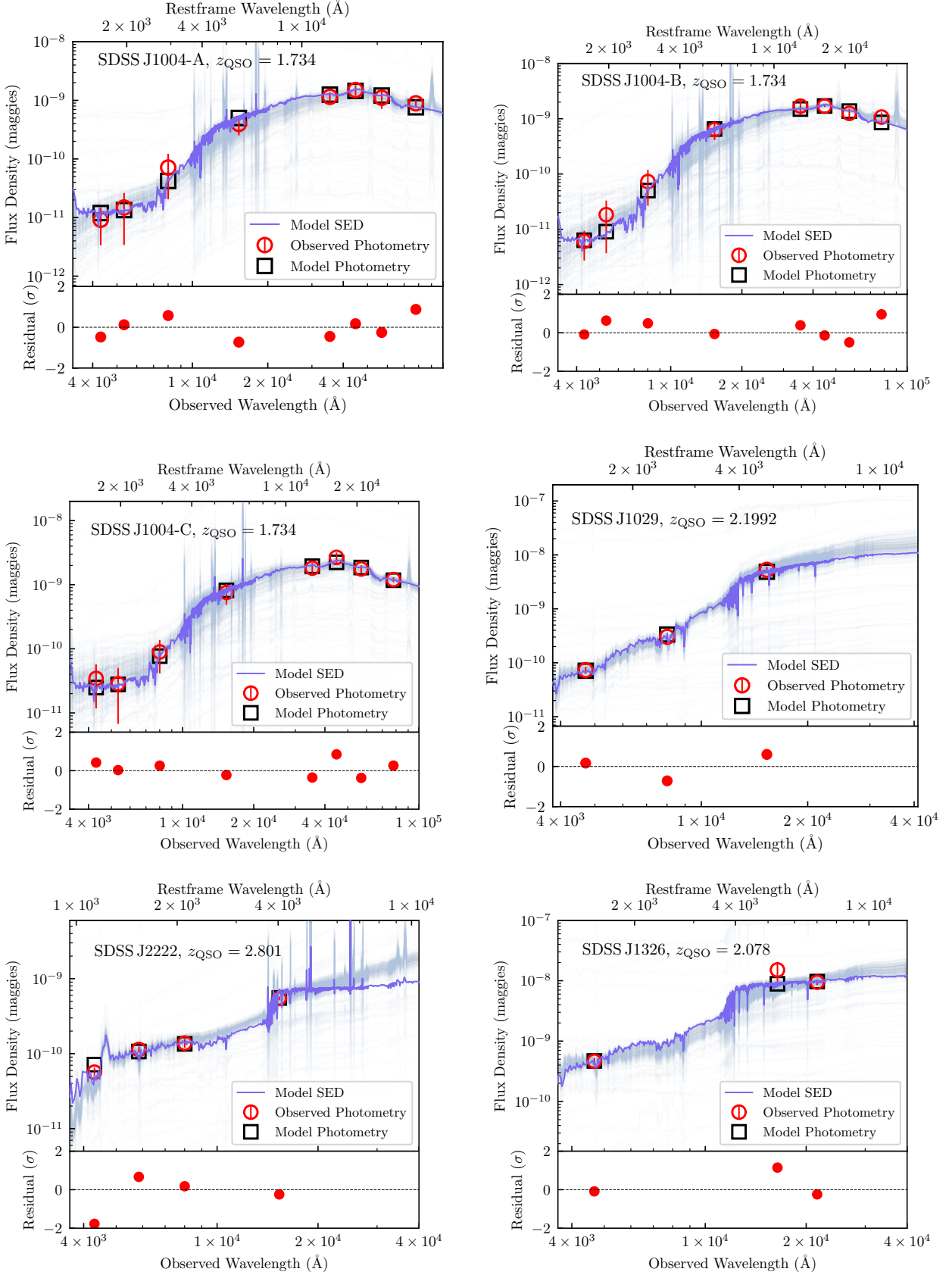


Figure B2. A gallery of host galaxy SEDs, computed using our SPS modeling framework described in Section 3.2. Similar to Figure B1, note that we model three separate images of the quasar host for each of SJ1004 and CJ1153 for testing systematics, with images A, B, and C visually defined in Figure 1.

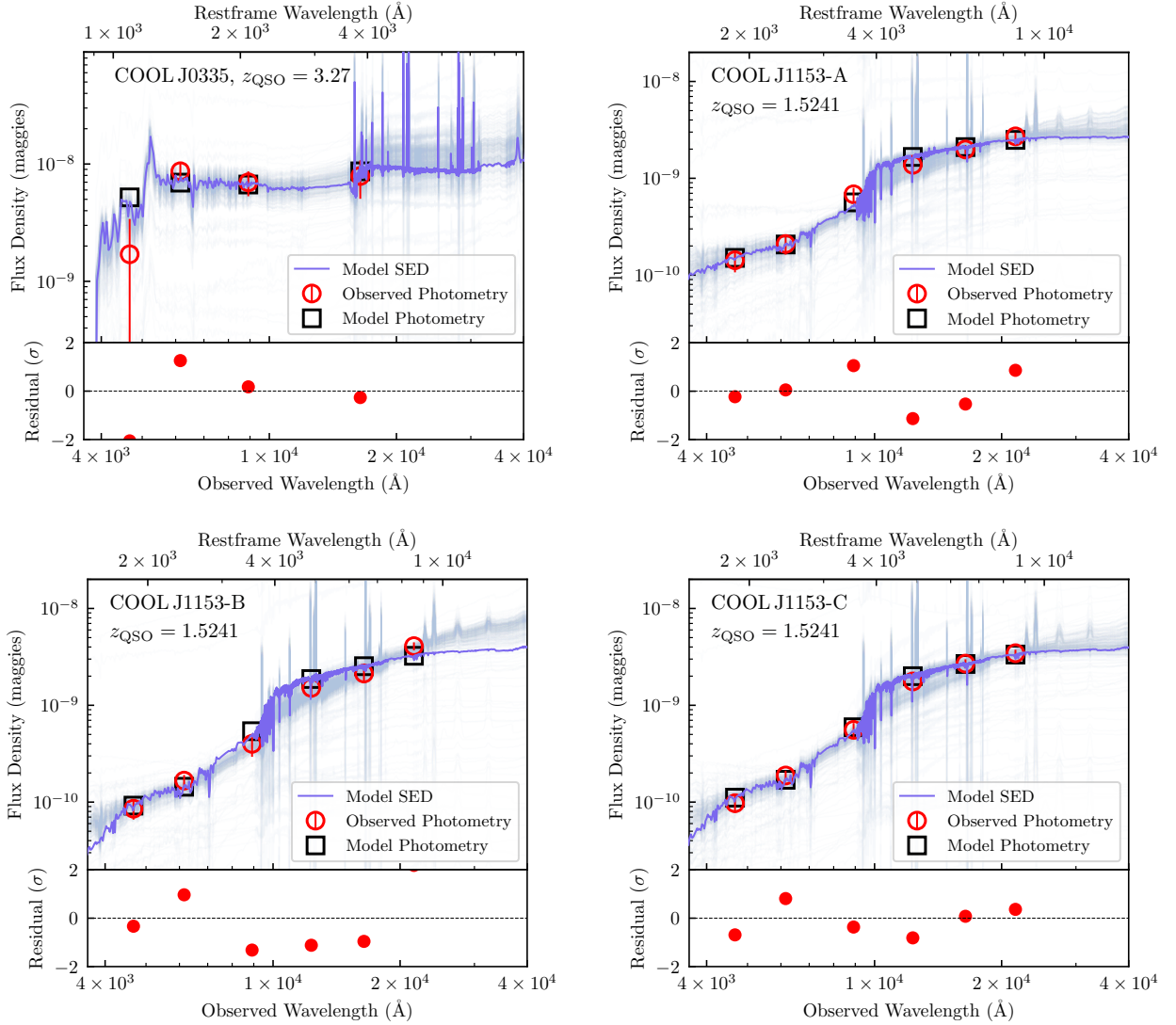


Figure B2. (continued) A gallery of host galaxy SEDs, computed using our SPS modeling framework described in Section 3.2. Similar to Figure B1, note that we model three separate images of the quasar host for each of SJ1004 and CJ1153 for testing systematics, with images A, B, and C visually defined in Figure 1.